

TOPICAL REVIEW

Synthetic aperture radar interferometry

Richard Bamler^{†§} and Philipp Hartl[‡][†] German Aerospace Center (DLR), Oberpfaffenhofen, D-82234 Wessling, Germany[‡] Institute of Navigation, University of Stuttgart, Geschwister-Scholl-Strasse 24D, D-70174 Stuttgart, Germany

Received 21 November 1997, in final form 28 February 1998

Abstract. Synthetic aperture radar (SAR) is a coherent active microwave imaging method. In remote sensing it is used for mapping the scattering properties of the Earth's surface in the respective wavelength domain. Many physical and geometric parameters of the imaged scene contribute to the grey value of a SAR image pixel. Scene inversion suffers from this high ambiguity and requires SAR data taken at different wavelength, polarization, time, incidence angle, etc.

Interferometric SAR (InSAR) exploits the phase differences of at least two complex-valued SAR images acquired from different orbit positions and/or at different times. The information derived from these interferometric data sets can be used to measure several geophysical quantities, such as topography, deformations (volcanoes, earthquakes, ice fields), glacier flows, ocean currents, vegetation properties, etc.

This paper reviews the technology and the signal theoretical aspects of InSAR. Emphasis is given to mathematical imaging models and the statistical properties of the involved quantities. Coherence is shown to be a useful concept for system description and for interferogram quality assessment. As a key step in InSAR signal processing two-dimensional phase unwrapping is discussed in detail. Several interferometric configurations are described and illustrated by real-world examples. A compilation of past, current and future InSAR systems concludes the paper.

1. Introduction

In the late 1970s spaceborne imaging radars began to play an important role in remote sensing, first for investigation of planetary surfaces, and later with the NASA satellite SEASAT, which was launched in 1978, for Earth observation (Allan 1983, Elachi 1991, Raney 1982b). It was demonstrated by the early missions that synthetic aperture radar (SAR) is able to reliably map the Earth's surface and acquire information about its physical properties, such as topography, morphology, roughness and the dielectric characteristics of the backscattering layer. SAR can be most beneficially used over land, ice and sea surfaces. As the spaceborne SAR systems operate in the microwave (cm to dm wavelength) regime of the spectrum and provide their own illumination they can acquire information globally and almost independently of meteorological conditions and sun illumination. They are, therefore, most suitable for operational monitoring tasks. The side-looking imaging geometry, pulse compression techniques as well as the synthetic aperture concept are employed to achieve geometric resolutions in the order of some metres to tens of metres with physical antennas of modest size as will be explained below. The price to be paid

§ E-mail address: Richard.Bamler@dlr.de

for such favourable performance is high transmit power, considerable amount of signal processing, and—compared to optical imagery—‘unconventional’ imaging geometry.

The use of spaceborne SARs as interferometers (interferometric SAR = InSAR or IFSAR) became popular only recently, although the basic principle dates back to the early 1970s (Graham 1974, Richman 1971). However, in view of terrestrial applications it was only in the 1980s that the first results were published (Gabriel and Goldstein 1988, Gabriel *et al* 1989, Goldstein *et al* 1989, Goldstein and Zebker 1987, Goldstein *et al* 1988, Prati *et al* 1989, Zebker and Goldstein 1986). As far as spaceborne InSAR is concerned only few well-selected SAR data sets of the 1978 SEASAT mission were at hand at that time. However, after the launch of the ESA satellite ERS-1 in 1991 an enormous amount of SAR data sets suitable for interferometry became available and a series of research groups began to investigate the method intensively and with success.

Today it is generally appreciated that SAR interferometry is an extremely powerful tool for mapping the Earth’s land, ice and even the sea surface topography. The so-called differential InSAR method (D-InSAR) represents a unique method for detection and mapping of surface displacements over large temporal and spatial scales with precision in the cm and even mm range. This is of great importance for earthquake and volcanic research, glaciology and ice sheet monitoring, studying tectonic processes, monitoring land subsidence due to mining, gas, water, and oil withdrawal, etc. Repeat-pass interferometry allows the detection and mapping of changes of spatial and/or dielectric properties of the land surface by using the temporal and spatial coherence characteristics, which can be successfully used for land cover classification, mapping of flooded areas, monitoring of geophysical parameters, etc.

The purpose of this paper is to review the methods of SAR interferometry and to describe aspects concerning the inverse problem of extracting qualitative and quantitative information requested in geoscience and for practical use from the acquired interferometric data. This paper shall stimulate experts in the field of inverse problems to deal more deeply with this matter.

It is necessary to first describe the basics of SAR imaging and explain its features. Section 2 gives a sufficient understanding of this and the various methods of SAR interferometry and the involved capabilities and constraints. Section 3 deals with InSAR itself. The main emphasis is put on across-track InSAR, but the mathematical modelling is kept very general, thus providing enough background to enable the reader to also comprehend other interferometric configurations. The main parameters used in InSAR will be discussed.

Section 4 is devoted to a central problem of InSAR signal processing: two-dimensional (2D) phase unwrapping. Section 5 reviews various interferometric configurations and includes some examples. In section 6, the current and future interferometric SAR systems are briefly described.

2. Synthetic aperture radar imaging

2.1. SAR data acquisition

For the purpose of this paper it is sufficient to intuitively understand the basics of SAR imaging; subtleties not essential to SAR interferometry will be generously omitted here. All equations in this section will be given in their simplest possible form; they can be readily generalized should some of the underlying assumptions require revision.

As any non-trivial imaging method, SAR is a two-step procedure. The raw data acquired by a coherent radar resemble a hologram rather than an image and, hence, require

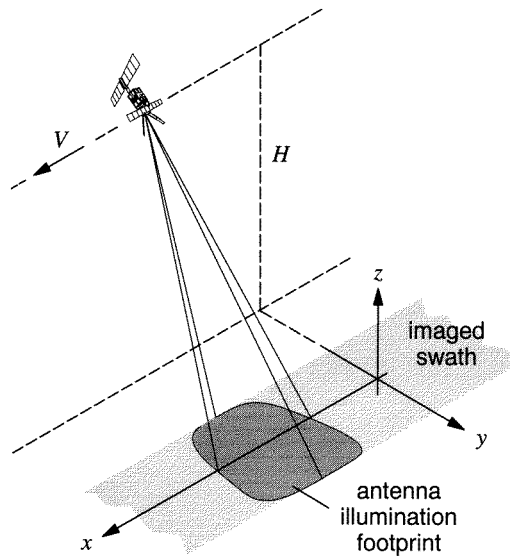


Figure 1. SAR imaging geometry. Frequently used terms are ‘along-track’ or ‘azimuth’ for x , ‘ground range’ for y , and ‘slant range’ for the distance of a particular point from the SAR sensor.

a considerable amount of signal processing for image formation (or ‘focusing’). SAR data processing is an interesting inverse problem itself. Particularly, the non-stationarity of the required operations and the possibly huge extent of the involved correlation kernels is still a challenge when it comes to real-time or on-board implementation. The theoretic aspects of SAR systems and image focusing are quite well understood and there is a rich selection of publications on various algorithms and implementations to which the obliged reader is referred (Bamler 1992, Bamler and Schättler 1993, Barber 1985, Blackledge 1987, Boone *et al* 1989, Brown 1967, Brown and Porcello 1969, Cafforio *et al* 1991, Curlander 1982, Curlander and McDonough 1991, Davidson and Cumming 1997, Davidson *et al* 1996, Di Cenco 1988, Elachi 1988, 1991, Franceschetti and Schirinzi 1990, Gough and Hawkins 1997, Harger 1970, Haykin 1985, Jin and Wu 1984, Li and Johnson 1983, McDonough *et al* 1985, Raney 1980, 1982a, Raney *et al* 1994, Raney and Vachon 1989, Rocca *et al* 1989, Runge and Bamler 1992, Scheuer and Wong 1991, Tomiyasu 1978, 1981, Wu *et al* 1982).

A—spaceborne or airborne—SAR illuminates the Earth’s surface in a side-looking fashion as depicted in figure 1. While the sensor is moving along its—assumed straight—path at an altitude H above some reference (x, y) -plane it transmits microwave pulses into the antenna’s illumination footprint at the rate of the *pulse repetition frequency* (PRF) and receives the echoes of each pulse scattered back from the Earth. The SAR receiver detects the stream of echoes coherently and separates it into individual echoes, each corresponding to a transmitted pulse. For processing the echoes are preferably arranged ‘side-by-side’ as a 2D matrix with coordinates ‘two-way signal delay time’ and ‘pulse number’. The pulse number relates to the satellite position along its flight path, the delay time to slant range.

Typical pulse carrier wavelengths used are approximately 3 cm (X-band), 6 cm (C-band), 9 cm (S-band), and 24 cm (L-band). Also 64 cm (P-band) might be used in the future. PRFs are in the range of 1–10 kHz.

For the moment, undisturbed wave propagation and noise-free reception are assumed.

Scattering may only occur in the vicinity of the reference plane within a layer bounded in height z , which covers the terrain to be imaged. The ensemble of scatterers is assumed to be temporarily stationary and to reside in the far-field of the SAR antenna. The antenna look direction will be perpendicular to the flight path, although this is never strictly true in real systems.

The commonly used SAR imaging geometry is known as (continuous) strip-map mode as shown in figure 1. We will primarily refer to this mode in this paper. Two other SAR mapping modes are of interest and will become important for future SAR systems: ScanSAR and spotlight mode.

As will be shown later, the SAR integration time, i.e. the duration a scatterer is illuminated by the radar, determines the azimuth (x -) resolution of the final image. In the strip-mode configuration of figure 1 the integration time is given by the azimuth extent of the antenna pattern. In ScanSAR mode (Ahmed *et al* 1990, Bamler and Eineder 1996, Cumming *et al* 1997, Monti Guarnieri and Prati 1996, Monti Guarnieri *et al* 1994, Moore *et al* 1981, Moreira *et al* 1996, Tomiyasu 1981) the integration time is deliberately shortened by operating the SAR in a bursted fashion, where it periodically transmits bunches of pulses (bursts). In the time between bursts the look angle of the antenna beam is changed in order to illuminate a swath parallel to the previous one. Following this routine the SAR sweeps its beam in a stepped manner from swath to swath before it returns to the first look direction. Hence, a ScanSAR system images several swaths temporarily interleaved quasi at the same time. During processing these swaths can be stitched together to give a total swath of up to 500 km width. The consequence of the enormous coverage is the reduced resolution due to the burst-mode operation.

The complimentary approach is adopted by spotlight SAR (Carrara *et al* 1995, Di Cenco 1988, Gough and Hawkins 1997, Munson *et al* 1983, Walker 1980). Here the antenna is continuously steered towards a certain patch on ground in order to keep it in view over a longer time. The increased integration time results in a higher azimuth resolution at the expense of coverage: a spotlight SAR can only image selected and isolated patches, while strip-mode and ScanSAR map strips of theoretically unlimited length.

In the following we will concentrate on strip-map SARs, but we will refer to special modes in section 6.

Obviously, two different scanning mechanisms are employed. Each transmitted pulse sweeps *across* the swath at the velocity of light. Simultaneously the scene is scanned in the *along-track* direction at the speed of the antenna footprint. The timescales of these two mechanisms differ from each other by several orders of magnitude, which allows us to treat them as mutually independent, an assumption often referred to as *start-stop approximation*. This suggests arranging the received echoes ‘side-by-side’ to form a raw data matrix, that may already be considered as a coarse image of the scattering object. The coordinates of the 2D raw signal representation—and of the later focused SAR image—are *range* R for the distance of the scatterer from the SAR (or equivalently *echo delay time*) and *azimuth* x for the position of the scatterer along the sensor path (cf figure 1). Synonyms often used are *cross-track* or *fast time* for range and *along-track* or *slow time* for azimuth.

The image characteristics of the raw data matrix are governed in the range direction by the radar principle and, hence, the range resolution is determined by the duration of the transmitted pulse (or by the inverse of its bandwidth, if phase-coded pulses are used). The raw data azimuth resolution, however, is limited (in the strip-map mode of figure 1) to the antenna footprint size which is in the order of $R\lambda/L$ and can be as large as several km (L is the length of the physical antenna in the flight direction. A typical value for spaceborne SARs is $L \cong 10$ m). Due to the coherent recording of the radar echoes in a SAR, the azimuth

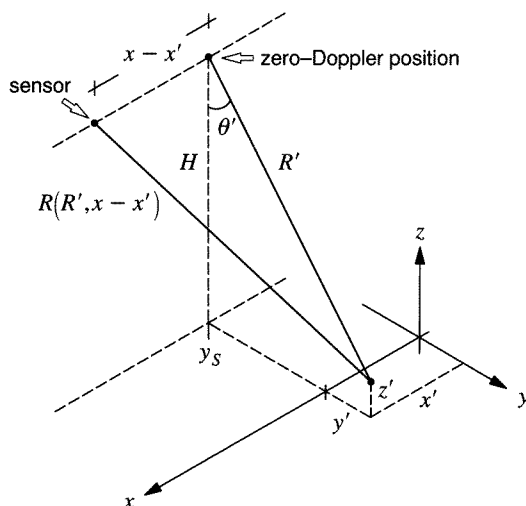


Figure 2. Range history $R(R', x - x')$ of a point scatterer.

phase history of every scatterer as it traverses the antenna beam is maintained. This phase history causes the (complex-valued) point scatterer response in the raw data to exhibit a highly oscillating structure when analysed in the azimuth direction (see below). It carries high-resolution information about the azimuth position of the scatterer. The smaller the antenna, i.e. the broader the azimuth antenna pattern, the more high-frequency components are contained in the azimuth point response. It can be shown that the azimuth spatial frequency bandwidth is in the order of $2/L$. Therefore, subsequent SAR data processing, which is essentially an all-pass (phase-only) filter operation, is able to focus the raw data to an azimuth resolution of about half the physical antenna length—independent of range, wavelength and sensor velocity.

For the derivation of the SAR imaging equations it is helpful to zero in on the response of a single point scatterer located at $(x, y, z)^T = (x', y', z')^T$. (Primed coordinates indicate a particular position of a point scatterer or of a scattering volume element under consideration.) Adopting the geometry of figure 2 the location of the point may also be given in cylindrical coordinates $(x', R', \theta')^T$. The position of the SAR sensor along its path is $(x, y_s, H)^T$.

Let $g(t)$ be the envelope of a single transmitted wavepackage and f_0 the radar carrier frequency. Then a transmitted pulse is (in complex analytic signal representation)

$$g(t) \exp\{j2\pi f_0 t\}. \quad (1)$$

$g(t)$ may be a short (i.e. high bandwidth) pulse like a rect-, a Gaussian, or a sinc-function; in order to avoid exceedingly high peak powers at the radar transmitter, long phase-coded pulses of the same bandwidth are more common instead, like chirps of the type $g(t) = \exp\{j\pi\beta t^2\}$.

The echoes returned from the point scatterer are delayed replicas of the transmitted signal:

$$g(t - 2R(R', x - x')/c) \exp\{j2\pi f_0(t - 2R(R', x - x')/c)\} \exp\{j\phi_{\text{scat}}\} \quad (2)$$

and finally after coherent (quadrature) demodulation:

$$g(t - 2R(R', x - x')/c) \exp\{-j2kR(R', x - x')\} \exp\{j\phi_{\text{scat}}\}. \quad (3)$$

Here inconsequential factors and constants have been omitted; c is the light velocity, $k = 2\pi/\lambda$ is the wavenumber and $\lambda = c/f_0$ the wavelength of the transmitted pulse, and ϕ_{scat} is a possible phase shift introduced by the scattering mechanism. The *range history* $R(\cdot, \cdot)$ is readily found for a rectilinear configuration as the one in figure 2:

$$R(R', x - x') = \sqrt{R'^2 + (x - x')^2} \quad (4)$$

where

$$R' = \sqrt{(y' - y_s)^2 + (H - z')^2}. \quad (5)$$

Equations (3)–(5) can be considered as the 2D point response of the SAR raw data acquisition system. Its azimuth support is given by the antenna footprint extent, often denoted *synthetic aperture*.

The range history has a two-fold effect. First, the pulse envelope $g(\cdot)$ is not exactly positioned at the same range time $t = 2R'/c$ for all azimuth values x ; it rather follows a hyperbolic trajectory in the raw data matrix. The deviation $\delta t = 2(R(\cdot, \cdot) - R')/c$ of the point response from a straight line in the raw data is known as *range cell migration*. It introduces a coupling between range and azimuth, makes the problem of SAR data processing non-separably 2D and requires a clear distinction between range time t and range R . However, for the purpose of this paper it can be neglected. Secondly, the range history is transformed into an azimuth-dependent phase history in a very sensitive way; for example a range variation of half a wavelength results in a full phase cycle. SAR processing exploits this rapidly varying high bandwidth phase structure and performs a deconvolution in the azimuth direction to resolve different scatterers within the synthetic aperture. The final SAR image is a function of azimuth x and range R . For the purpose of this paper it is convenient to assume that the processing filters have been designed so as to focus the response of a scatterer at its *zero-Doppler coordinates*. They are defined as the very range and azimuth where the sensor and scatterer are closest to each other, i.e. where $\partial R/\partial x = 0$ and, hence, $x = x'$ and $R = R'$; other coordinate systems are possible (Curlander 1982).

(The term ‘zero-Doppler’ is inherited from classical radar theory employing the concept of Doppler frequency shift which is actually not useful here.)

2.2. Space domain SAR imaging system model

For our purposes it is sufficient to view SAR data acquisition and processing as a single operator describing the *end-to-end system* characterized by its point response. Consider a (zero-phase) point scatterer located in three-dimensional (3D) space again located at $(x, y, z) = (x', y', z')$:

$$\delta(x - x', y - y', z - z'). \quad (6)$$

As discussed above, its response in the (complex-valued) SAR image will be centred at its zero-Doppler coordinates:

$$h(x - x', R - R') \cdot \exp\{-j2kR'\}. \quad (7)$$

Here $h(x, R)$ is the 2D range and azimuth impulse response function. In the following we will often assume simple rectangular filter functions of bandwidths W_R and W_x in range and azimuth, respectively; then $h(x, R) = \text{sinc}(W_x x) \text{sinc}(W_R R)$. The (spatial) range bandwidth W_R is related to the (time) bandwidth W_g of the transmitted waveform via $W_R = 2W_g/c$ while the azimuth bandwidth W_x is in the order of $2/L$.

At this stage of processing the synthetic aperture aspect of SAR is no longer visible; the end-to-end system can be thought of as a straightforward yet high-resolution scanning

radar. This view is only applicable if the scatterer has not moved while it was illuminated, an assumption that is not true for moving target indication radars or for imaging of the ocean surface; see e.g. Alpers *et al* (1981), Hasselmann and Hasselmann (1991), Krogstad (1992), Lyzenga (1986), Milman *et al* (1993), Ouchi and Burridge (1993), Plant (1992), Raney (1980), Raney and Vachon (1988), Tomiyasu (1978) and Vachon *et al* (1994).

In order to arrive at a conveniently simple mathematical model of SAR imaging we need another, yet quite restrictive, assumption: *linearity*. It means that the scene to be imaged can be considered as an—arbitrarily dense—ensemble of individual point scatterers, whose scattered fields and, hence, their responses in the SAR image, superpose linearly. This is equivalent to the first Born approximation and excludes, for example, attenuation and multiple scattering. Let us call the 3D density of scatterers the *scattering object* $a(x, y, z)$ and use vector notation for compactness of the equations: $\mathbf{r} = (x, y, z)^T$ and $\mathbf{r}' = (x', y', z')^T$.

Under the first Born approximation, the linear operator characterizing the SAR imaging process is a geometric projection of $a(x, y, z)$ from 3D space into the 2D cylindrical zero-Doppler radar coordinates (x, R) followed by a 2D convolution with the point response of equation (7):

$$\begin{aligned} u(x, R) &= \int a(\mathbf{r}') \exp\{-j2kR'\} h(x - x', R - R') dV' \\ &= \left(\int a(\mathbf{r}) R d\theta \times \exp\{-j2kR\} \right) ** h(x, R) \end{aligned} \quad (8)$$

where ‘**’ stands for 2D convolution, $dV' = dx' dy' dz'$ and (cf figure 2):

$$y = y_S + R \sin \theta \quad z = H - R \cos \theta \quad (9)$$

where $u(x, R)$ denotes the SAR image and θ is the angle between the sensor-to-scatterer line and the z -axis (cf figure 2). Note that we use the terms ‘image’ and ‘pixel’ for complex-valued functions or values, although they are often associated with real non-negative functions. The coordinate R is also called *slant range* while y is known as *ground range*.

In the azimuth direction the imaging process is a simple low-pass filter convolution; it is not affected by the geometric projection. Therefore, in the subsequent figures we will concentrate on planes orthogonal to the flight path x (the *zero-Doppler planes*). Figure 3 illustrates equations (8) and (9) in the plane $x = 0$.

Trivially, due to the projection of $a(x, y, z)$ onto the cylindrical coordinates x and R , represented by the θ -integration along arcs of circles in equations (8) and (9), information about the scatterer’s spatial structure and location gets lost (which is similarly true also for optical imaging). All points located in the same zero-Doppler plane and having the same distance to the SAR, i.e. lying on a circle, cannot be distinguished from each other and will be mapped into the same SAR image pixel. We shall learn that SAR interferometry will provide us with information about the missing dimension, the incidence angle θ .

Fortunately, there is often considerable *a priori* knowledge about the scattering object. For example, the dominant scattering mechanism of most geologic objects at short wavelengths is *surface scattering*, reducing the projection to a distortion that can often be corrected for by backprojecting the SAR image onto a digital elevation model (DEM) of the terrain, if available. As can be concluded from figure 3 the distortion mentioned makes terrain slopes tilted towards the SAR appear contracted (*foreshortening*) in the image while those tilted away from the SAR get stretched. This lets mountains in SAR images look as if they are leaning towards the SAR sensor. Once the terrain slope angle is equal to or

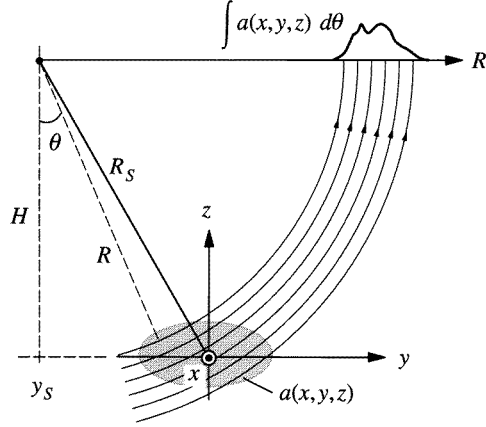


Figure 3. Illustration of equations (8) and (9).

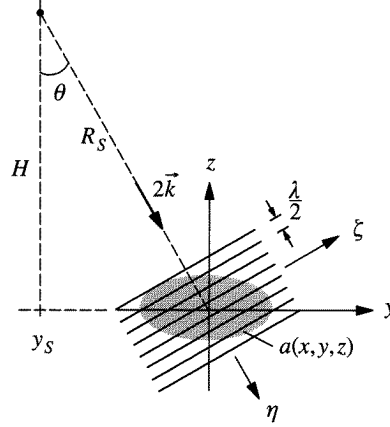


Figure 4. Illustration of the plane wave SAR imaging equation (12).

even exceeds the look angle θ the projection becomes ambiguous, for example a mountain peak may be mapped onto the same pixel as some point in the nearby valley. This effect is referred to as *lay-over*. Foreshortening and some lay-over can be observed near the ridges of the central mountain of figure 8 and in figure 11 (right). The other extreme is terrain slope angles $< \theta - 90^\circ$, where *radar shadow* is observed.

For the purposes of this paper it is helpful to develop a *plane wave approximation* of equation (8) by considering only a sufficiently small neighbourhood around an expansion point in space; without loss of generality we will choose $(x, y, z)^T = (0, 0, 0)^T$ for the expansion point. Then the projection circles in equations (8) and (9) may be approximated by straight lines, which is equivalent to replacing the cylindrical wave $\exp\{-j2kR\}$ in equation (8) by a plane wave $\exp\{-j2\mathbf{k} \cdot \mathbf{r}\}$ with wavevector $\mathbf{k} = k(0, \sin\theta, -\cos\theta)^T$.

Let us further assume that the origin of the range coordinate in the SAR image has been set at $R_S = \sqrt{H^2 + y_S^2}$ and define a new range coordinate η as

$$\eta = R - R_S. \quad (10)$$

Finally, we introduce an axis ζ orthogonal to the η -axis. η and ζ form a coordinate system in the object space that is rotated by $\theta - \pi/2$ with respect to y and z (figure 4):

$$\begin{pmatrix} y \\ z \end{pmatrix} = \begin{pmatrix} \sin\theta & \cos\theta \\ -\cos\theta & \sin\theta \end{pmatrix} \begin{pmatrix} \eta \\ \zeta \end{pmatrix}. \quad (11)$$

Then the *plane wave approximation* of equation (8) becomes

$$\begin{aligned} u(x, \eta) &\cong \exp\{-j2kR_S\} \int a(\mathbf{r}') \exp\{-2j\mathbf{k} \cdot \mathbf{r}'\} h(x - x', \eta - \eta') dV' \\ &= \exp\{-j2kR_S\} \left(\int a(\mathbf{r}) d\zeta \times \exp\{-j2k\eta\} \right) ** h(x, \eta) \\ &= \exp\{-j2k(R_S + \eta)\} \times \int a(\mathbf{r}) d\zeta ** (h(x, \eta) \times \exp\{j2k\eta\}) \end{aligned} \quad (12)$$

where $\mathbf{k} \cdot \mathbf{r}' = k\eta$ has been used and two alternative versions of the convolutional description have been explicitly outlined.

The leading constant phase factor and the convolution with the SAR point response are self-explaining. The integral is the essential operation: the scattering object is projected

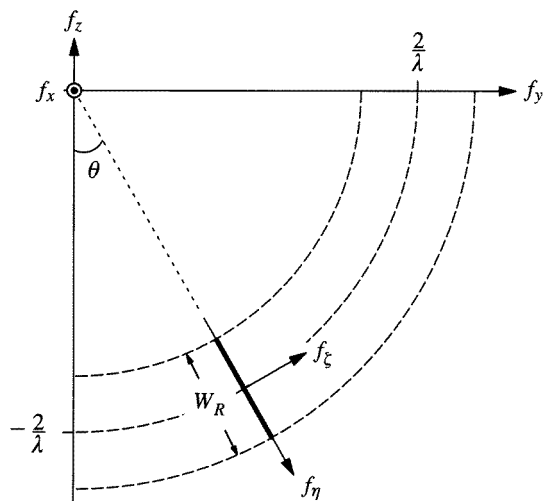


Figure 5. Fourier domain SAR imaging model (cf equations (13) and (14)) showing the slice (bold) of the object spectrum in the (f_y, f_z) -plane that is transferred to the SAR image. A rect-shaped range system transfer function of bandwidth W_R is assumed.

along ζ onto the η -axis. This is equivalent to tomography. Hence, a SAR image gives us a *single tomographic projection* of the object, band-pass filtered by the range frequency-shifted SAR point response function: $h(x, \eta) \times \exp\{j2k\eta\}$.

2.3. Frequency domain SAR system model

In order to understand how much information of $a(\mathbf{r})$ is transferred into the SAR image $u(x, \eta)$ a frequency domain system model is helpful (Cafforio *et al* 1991, Gatelli *et al* 1994). The convolutional tomographic formulation from equation (12) is readily transformed into the spectral domain using the well known Fourier projection central slice theorem:

$$U(f_x, f_\eta) \cong \exp\{-j2kR_S\}A(f_x, f_y, f_z)H(f_x, f_\eta) \quad (13)$$

where the transfer function $H(f_x, f_\eta)$ is confined to the plane given by

$$f_y = \left(f_\eta + \frac{2}{\lambda}\right) \sin \theta \quad f_z = -\left(f_\eta + \frac{2}{\lambda}\right) \cos \theta. \quad (14)$$

We use capital letters to denote Fourier transforms, e.g. $U(f_x, f_\eta) = \iint u(x, \eta) \cdot \exp\{-j2\pi(f_x x + f_\eta \eta)\} dx d\eta$.

Obviously, the SAR image spectrum is a single 2D *slice* out of the 3D object spectrum as illustrated in figure 5.

2.4. SAR image statistics

According to equation (12) we have modelled SAR imaging as a convolution of the—phase-shifted and projected—scattering object with a low-pass impulse response function. This description is sufficient, if we can assign a unique object function to every physical scene to be imaged. Since the phase term in the projection operator of equation (12) is extremely sensitive to range, the location of every scatterer in a resolution element (tens of metres) has to be known to within a small fraction of a wavelength (centimetres)—a requirement

never met for natural *distributed scenes* like rough surfaces. These scenes are adequately described by their so-called backscatter coefficient, which is a measure of the *expectation value* of backscattered *power*. Hence, there are arbitrarily many realizations leading to the same backscatter coefficient, and the scattering object function as well as the SAR image are preferably treated as random processes.

We will restrict ourselves to the two extreme cases of scattering objects: point scatterers and Gaussian (or Rayleigh) scatterers. The response of a point scatterer is well described by equation (7).

Gaussian scatterers are those that can be decomposed into a sufficiently high number of random subscatterers within a resolution cell. It is necessary that no single subscatterer remarkably dominates the others. If these conditions are met, the central limit theorem will apply and the SAR image pixel value $u(x, \eta)$ is a complex *circular Gaussian* random variable. For medium resolution (tens of metres) spaceborne remote sensing SARs the Gaussian assumption is true for most natural scatterers such as forests, agricultural fields, rough water, soil or rock surfaces. It is violated, if only few dominant scatterers are present in a resolution cell such as artificial objects, urban areas or with high-resolution SAR systems.

We assume that the object function is a white random process with autocorrelation function

$$R_{aa}(\mathbf{r}_1, \mathbf{r}_2) = E[a(\mathbf{r}_1)a^*(\mathbf{r}_2)] = \sigma_v(\mathbf{r}_1)\delta(\mathbf{r}_1 - \mathbf{r}_2) \quad (15)$$

where $\sigma_v(\mathbf{r})$ is the *volumetric backscatter coefficient* (Askne *et al* 1997, Ulander and Hagberg 1995). It represents the radar cross section per unit volume and is measured in $\text{m}^2 \text{m}^{-3}$. Using the special form of $R_{aa}(\cdot, \cdot)$ the expected value of the *pixel intensity* is found as

$$\begin{aligned} \bar{I}(x, \eta) &= E[|u(x, \eta)|^2] = \int \sigma_v(\mathbf{r}') |h(x - x', \eta - \eta')|^2 dV' \\ &= \left(\int \sigma_v(\mathbf{r}) d\zeta \right) ** |h(x, \eta)|^2. \end{aligned} \quad (16)$$

In the case of pure *surface scattering* (e.g. at $z = 0$) the dimensionless backscatter coefficient $\sigma^0(\cdot)$ describes the object:

$$\sigma_v(\mathbf{r}) = \sigma^0(x, y)\delta(z) \quad (17)$$

and the expected value of the pixel intensity is

$$\bar{I}(x, \eta) = \frac{\sigma^0(x, \eta/\sin\theta)}{|\sin\theta|} ** |h(x, \eta)|^2. \quad (18)$$

Under the assumption of circular Gaussian image statistics the probability density function of a complex image pixel u is

$$pdf(u) = \frac{1}{\pi \bar{I}} \exp \left\{ -\frac{(\text{Re}\{u\})^2 + (\text{Im}\{u\})^2}{\bar{I}} \right\}. \quad (19)$$

(For simplicity of notation we use the same symbol ‘ u ’ for both the random variable and a single pixel value.)

Several conclusions can be drawn from equation (19). Real and imaginary parts of u are mutually uncorrelated. Also, phase and magnitude are uncorrelated. Obviously, there is no information in the phase of a single image pixel of a Gaussian scatterer; the *pdf* of the

phase is uniform due to the summation over many scatterers of random phase. The *pdfs* of the pixel intensity and magnitude, however, are pronounced:

$$pdf(I) = \frac{1}{\bar{I}} \exp\left\{-\frac{I}{\bar{I}}\right\} \quad \text{where } I = |u|^2 \quad (20)$$

$$pdf(M) = \frac{2M}{\bar{I}} \exp\left\{-\frac{M^2}{\bar{I}}\right\} \quad \text{where } M = |u|. \quad (21)$$

The fluctuations of pixel intensities described by these *pdfs* are known as the *speckle effect* in the context of coherent imaging of rough surfaces (see, e.g. Dainty (1975), Goodman (1976), Madsen (1986, 1987)). Speckle is often misleadingly blamed as ‘noise’, although the speckle pattern of the imaged object contains information about its subresolution structure. Of course, when it comes to estimation of the backscatter coefficient from a single SAR image speckle is a nuisance.

3. SAR interferometry

Many different flavours of SAR interferometry have recently been developed rendering an exact definition of InSAR difficult. We will use the term *SAR interferometry* for all methods that employ at least two complex-valued SAR images to derive more information about the object than present in a single SAR image by exploiting the *phase* of the SAR signals. For a second SAR image to provide additional information at least *one* imaging parameter must be different compared with the first image. Which parameter this is (e.g. flight path, acquisition time, wavelength) determines the type of the interferometer. In section 5 some InSAR configurations will be discussed. Since the best known application of InSAR is the reconstruction of the Earth topography by *across-track interferometry*, we will use it as an example in this section.

3.1. Across-track interferometer

Let us approximate the scattering object for the moment by a surface describing the Earth topography. According to figure 3 SAR imaging projects the scattering object along circles, i.e. the (y, z) -location of every surface point is reduced to range R in the SAR image. Across-track interferometry is a means to measure the look angle θ as a second coordinate and thus allows us to recover the point’s location in space. The configuration resembles a stereo arrangement (figure 6): two SARs fly on (ideally) parallel tracks and view the terrain from slightly different directions. The separation of the flight paths is called *baseline* B , its component perpendicular to some look direction the *effective baseline* B_{\perp} . Given the sensor locations and the two ranges R_1 and R_2 every point of the Earth’s surface can be mapped back into space by triangulation. Unlike conventional stereo techniques, where homologous points must be identified and image contrast is required, interferometry uses the phase information of *every* pixel to measure the parallax $\Delta R = R_2 - R_1$.

As sketched in figure 6, across-track interferometry requires two SAR antennas operated simultaneously (single-pass interferometry). Many configurations use a single SAR system and image the area twice from slightly different orbits at different times (repeat-pass interferometry).

Let

$$u_1(R, x) = |u_1(R, x)| \exp\{j\phi_1(R, x)\} \quad \text{and} \quad u_2(R, x) = |u_2(R, x)| \exp\{j\phi_2(R, x)\} \quad (22)$$

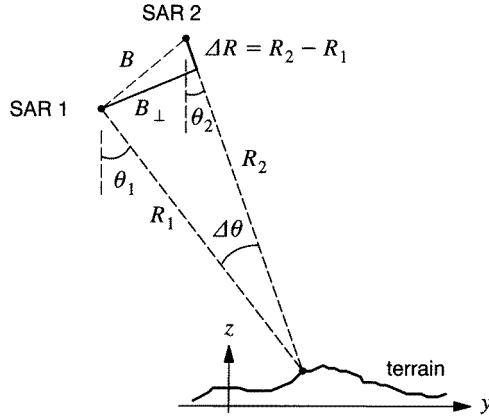


Figure 6. Across-track SAR interferometer (flight paths perpendicular into plane).

be the two SAR images forming the *interferogram*

$$v(\cdot) = u_1(\cdot)u_2^*(\cdot) = |u_1(\cdot)||u_2(\cdot)| \exp\{j\phi(\cdot)\} \quad (23)$$

where

$$\phi(\cdot) = \phi_1(\cdot) - \phi_2(\cdot) \quad (24)$$

is the *interferometric phase*.

Referring to equation (7), the phase of the SAR image response of a point scatterer is proportional to range plus a possible shift due to the scatterer itself, i.e.

$$\phi_1 = -2kR_1 + \phi_{\text{scat},1} \quad \text{and} \quad \phi_2 = -2kR_2 + \phi_{\text{scat},2}. \quad (25)$$

Assuming that the scattering phase is the same in both images the interferogram phase is a very sensitive measure for the range difference:

$$\phi = 2k\Delta R = \frac{4\pi}{\lambda} \Delta R. \quad (26)$$

Of course, ϕ is still ambiguous to within integer multiples of 2π . We will address the problem of phase unwrapping in section 4. Once ΔR has been measured, the point's location in the zero-Doppler plane is found as the intersection of the circle $R = \text{constant}$ and a hyperbola defined by $\Delta R = \text{constant}$. (Due to reasons to be explained later, the baseline is small enough that—after coregistration of the SAR images— $R = \text{constant}$ defines the same circle for both SARs to within the range resolution width.) Figure 7 shows the interference pattern of the iso-phase circles of the two SAR images; the lines of equal phase difference are orthogonal to these circles. Hence, in a small neighbourhood of a point the range R and the range difference ΔR form an orthogonal coordinate system, where ΔR is the dimension that was missing so far. In comparison with figure 4, ΔR is related to ζ via

$$\zeta \cong \frac{R_S}{B_\perp} \Delta R. \quad (27)$$

This second coordinate can also be considered as a measure of look angle θ .

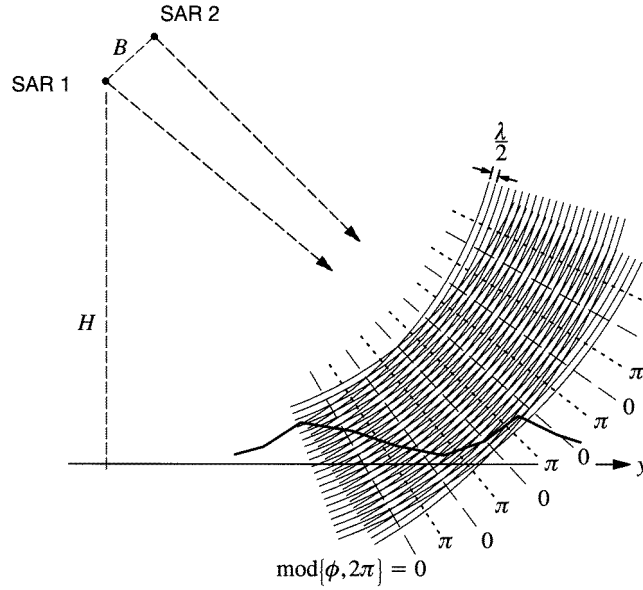


Figure 7. Interference of iso-phase lines.

3.2. Interferogram example

Figures 8 and 9 show a SAR image together with the interferogram of the same area in the Mojave Desert, CA, USA. It is a rather flat plain with mountainous parts. In the SAR intensity image, figure 8, the mountains exhibit the geometric distortions discussed earlier; they tend to ‘lean’ towards the sensor (foreshortening) which imaged the area from the top. The interferometric phase in figures 9 and 10 is coded in colour. The iso-phase contours form a pattern that is usually referred to as *fringe* pattern. It consists of a dominant frequency in the range direction locally distorted by terrain height variations. The general phase trend in range can be considered as the phase generated by an ideally flat Earth and is often subtracted from the interferogram before further processing (figure 10). Flattened like this the resulting fringe pattern already resembles iso-height contours. Where the terrain is essentially flat the fringe spacing is large, indicating low height variation. The mountain in the centre of the scene gives rise to narrow fringe lines. About 13 fringes can be counted from the base to the top of the mountain; with the given imaging geometry this amounts to a height of approximately 975 m.

The following are useful equations all based on the first-order expansion from equation (27). The *height sensitivity* of the interferometer is

$$\frac{\partial \phi}{\partial z} = \frac{4\pi}{\lambda} \frac{B_{\perp}}{R_s \sin \theta}. \quad (28)$$

Often, the *height of ambiguity* $z_{2\pi} = \frac{\lambda}{2} \frac{R_s \sin \theta}{B_{\perp}}$, i.e. the height resulting in a phase change of one fringe (2π), is used in place of $\partial \phi / \partial z$ to characterize the sensitivity of the interferometer. The *local fringe frequency* in range is a key parameter of the interferometer:

$$f_{\phi} = \frac{1}{2\pi} \frac{\partial \phi}{\partial R} = -\frac{2B_{\perp}}{\lambda R_s \tan(\theta - \alpha)} \quad (29)$$

where α is the terrain slope component in the zero-Doppler plane (positive for slopes tilted towards the SAR sensor).

3.3. Spectral description of across-track interferometry

So far we have seen that the 3D (x, η, ζ) -position of a single-point scatterer can be obtained from the interferogram and rotated back into (x, y, z) -space via equation (11). These findings do not provide us with sufficient insight to explain interferometric responses of real-world scattering objects where many scatterers are present in every resolution element (e.g. Gaussian scattering). Rather than viewing InSAR as a means to triangulate single points we must consider it as an *imaging process* that attempts to measure the 3D structure of an object.

In section 2 we learnt that a single SAR image gives us a 2D projection of the 3D scattering object or, according to equations (13) and (14) and figure 5, a slice out of the object's spectrum. *Two* SAR images, however we combine them, can only give us *two* projections or *two* spectral slices (figure 19). Hence, if real 3D imaging was our aim much more than two SAR images must be employed (Fortuny *et al* 1994, Gatelli *et al* 1994, Prati and Rocca 1993) and/or *a priori* knowledge about the object is required.

How can we hope then to reconstruct the shape of the Earth's surface from a single interferogram? Of course, such a limited set of projections can never describe an arbitrary scattering configuration. In terrain reconstruction, however, the scattering layer is usually thin in the z -direction, i.e. the object spectrum is highly correlated in f_z and can be accurately modelled by a few moments. Then the two spectral slices shown in figure 19 can be sufficient to infer the principal shape of the object spectrum in f_z . This kind of inference is performed when the 3D position of the scattering centre of each resolution cell is determined by use of interferometric phase differences as described above.

3.4. Interferometric imaging model

Now we are ready to establish a system theoretical model of the interferometric imaging process for Gaussian scatterers (figure 20). Input is the scattering object. Since the two SAR images have not necessarily been acquired at the same time (repeat-pass interferometry), the scatterer may have changed between acquisitions and we need to consider two different objects $a_1(\mathbf{r})$ and $a_2(\mathbf{r})$ with cross-correlation function (cf equation (15))

$$R_{a_1 a_2}(\mathbf{r}_1, \mathbf{r}_2) = E[a_1(\mathbf{r}_1)a_2^*(\mathbf{r}_2)] = \sigma_{ve}(\mathbf{r}_1)\delta(\mathbf{r}_1 - \mathbf{r}_2) \quad (30)$$

where $\sigma_{ve}(\mathbf{r})$ is the volumetric backscatter coefficient of scatterers common to both objects. It can be interpreted as the temporarily stable scattering contribution (Askne *et al* 1997, Ulander and Hagberg 1995); scatterer contributions that have changed between observations average out in the expectation value and will not show up in $R_{a_1 a_2}(\mathbf{r}_1, \mathbf{r}_2)$. Note that this is only true for *random* changes of scatterers. Hence, this form of the cross-correlation function is not applicable for objects that perform a rigid movement and whose scattering properties remain stable. It is appropriate in the context of across-track InSAR, but requires refinement for along-track or differential interferometry. The two different objects $a_1(\mathbf{r})$ and $a_2(\mathbf{r})$ pass (possibly different) SAR systems, modelled as filters with point responses $h_1(x, \eta)$ and $h_2(x, \eta)$ according to equation (12). Finally, we consider mutually uncorrelated system noise $n_1(x, \eta)$ and $n_2(x, \eta)$ of intensity $E[|n_1|^2] = N_1$ and $E[|n_2|^2] = N_2$, respectively.

We will now employ the plane wave approximation from equation (12) to find the expected interferometric response of an arbitrary Gaussian scatterer configuration. We must consider the fact that the two SAR images have been acquired under different look angles, and, hence their (η, ζ) -coordinate systems are slightly different. However, the difference in look angle $\Delta\theta = \theta_1 - \theta_2 \cong B_\perp/R_S$ is small enough that we may use a single (η, ζ) -system oriented at $\theta = (\theta_1 + \theta_2)/2$. It is only the exponential factor $\exp\{-j2\mathbf{k} \cdot \mathbf{r}'\}$ in equation (12)

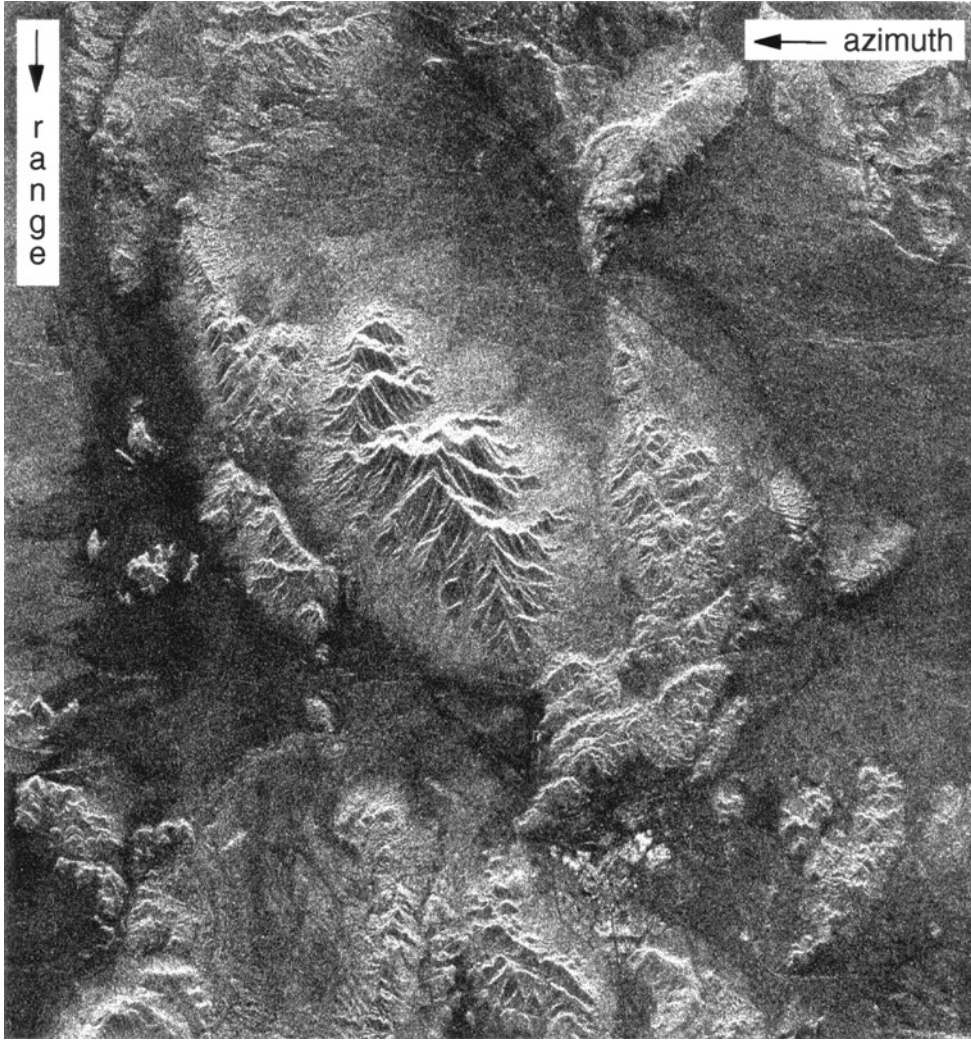


Figure 8. SAR magnitude image $|u_1|$ of an area in Mojave Desert, CA (approximately $25 \text{ km} \times 25 \text{ km}$). Two such images taken from slightly different orbit positions are used to form the interferograms of figures 9 and 10. Sensor: ERS-1/2 ©ESA.

that requires a distinction between the two wavevectors. Using equation (30) the *expected interferometric* response is finally found as (figure 21)

$$\begin{aligned}
 E[v(x, \eta)] &= E[u_1(x, \eta)u_2^*(x, \eta)] \\
 &= \exp\{-j2(k_1 R_{S1} - k_2 R_{S2})\} \int \sigma_{ve}(\mathbf{r}') h_1(x - x', \eta - \eta') h_2^*(x - x', \eta - \eta') \\
 &\quad \times \exp\{-j2(\mathbf{k}_1 - \mathbf{k}_2) \cdot \mathbf{r}'\} dV'.
 \end{aligned} \tag{31}$$

For the sake of generality we allow that the two images are possibly acquired using slightly different wavelengths, i.e. $k_1 \neq k_2$. The following expansion of the exponent will prove

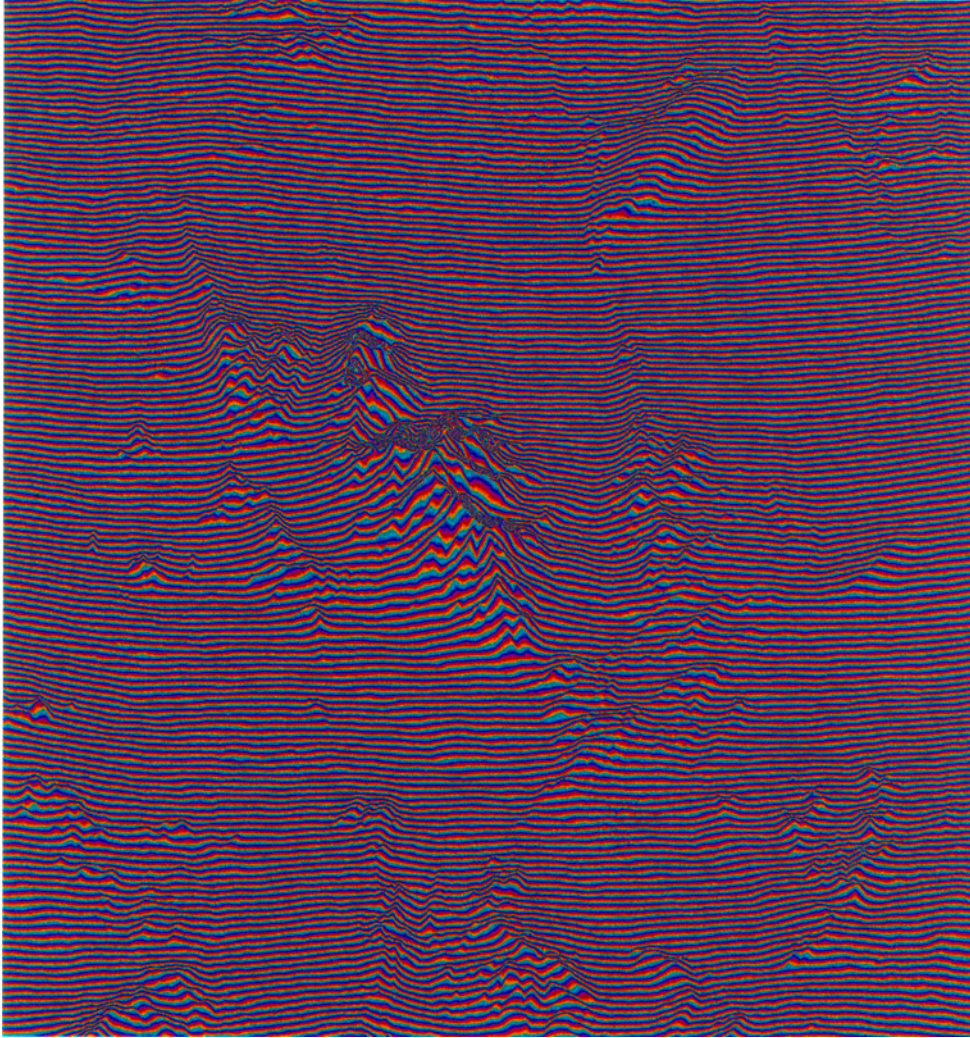


Figure 9. SAR interferogram of the area shown in figure 8. Raw interferometric phase ϕ in colour wheel representation. Sensor: ERS-1/2 ©ESA. Baseline: $B_{\perp} \cong 133$ m $\Rightarrow z_{2\pi} \cong 75$ m.

helpful:

$$(\mathbf{k}_1 - \mathbf{k}_2) \cdot \mathbf{r}' \cong k \Delta \theta \zeta' + \Delta k \eta' \cong k \frac{B_{\perp}}{R_S} \zeta' + \Delta k \eta' \quad (32)$$

where $k = 2\pi/\lambda = (k_1 + k_2)/2$ is the mean wavenumber of the two SAR systems and $\Delta k = k_1 - k_2$ is their wavenumber difference.

3.5. First-order interferogram statistics

In section 2 we introduced Gaussian scattering as a mathematically tractable model for distributed scatterers. Accepting this idealization we are able to give analytic expressions for the probability distributions of interferograms and related entities. The following collection of often used *pdfs* is given without derivation.

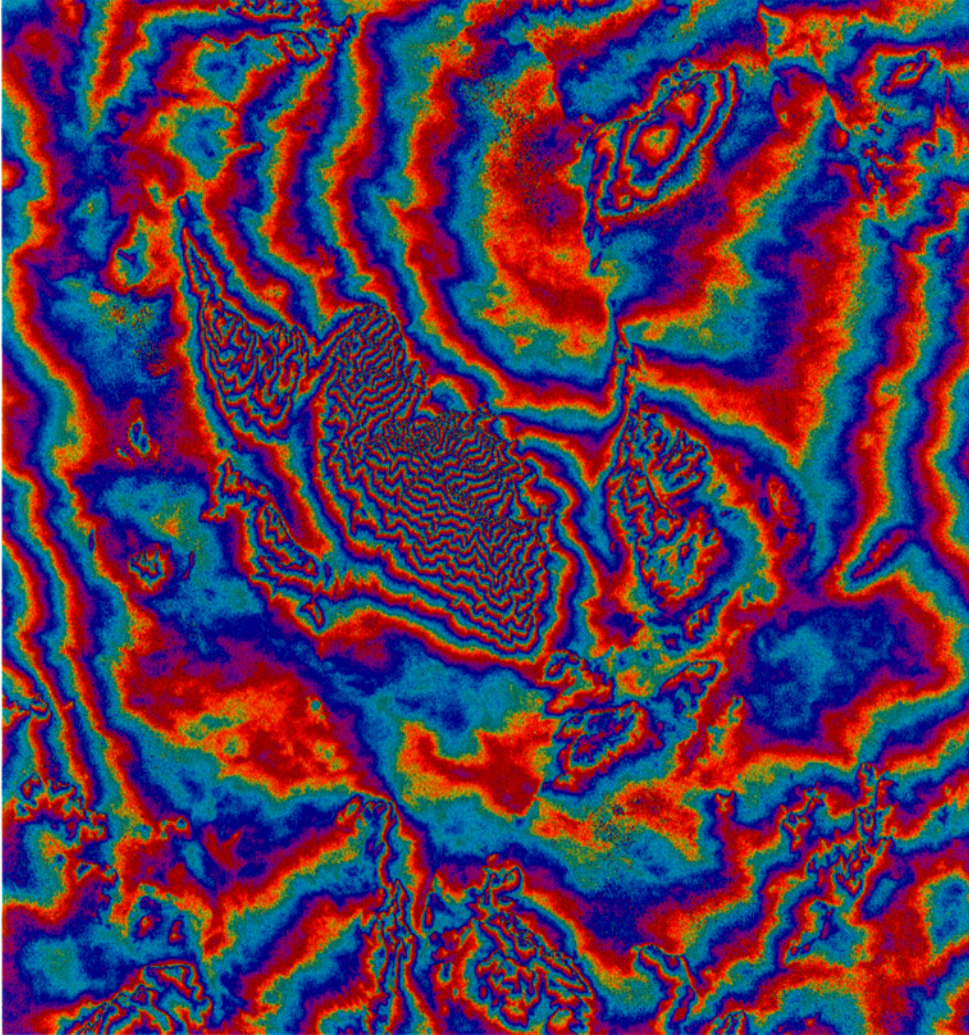


Figure 10. SAR interferogram of the area shown in figure 8. Interferometric phase of figure 9 after removal of flat Earth phase contribution. Sensor: ERS-1/2 ©ESA. Baseline: $B_{\perp} \cong 133$ m $\Rightarrow z_{2\pi} \cong 75$ m.

The processes u_1 and u_2 are assumed to be jointly circular Gaussian. Hence, their joint *pdf* is given by

$$pdf(\mathbf{w}) = \frac{1}{\pi^2 |\mathbf{C}|} \exp\{-\mathbf{w}^{*T} \mathbf{C}^{-1} \mathbf{w}\} \quad (33)$$

where

$$\mathbf{w} = \begin{pmatrix} u_1 \\ u_2 \end{pmatrix} \quad (34)$$

and, introducing $\bar{I} = \sqrt{\bar{I}_1 \bar{I}_2} = \sqrt{E[|u_1|^2]E[|u_2|^2]}$, the covariance matrix is

$$\mathbf{C} = E[\mathbf{w}\mathbf{w}^{*T}] = \begin{pmatrix} \bar{I}_1 & \gamma \bar{I} \\ \gamma^* \bar{I} & \bar{I}_2 \end{pmatrix}. \quad (35)$$

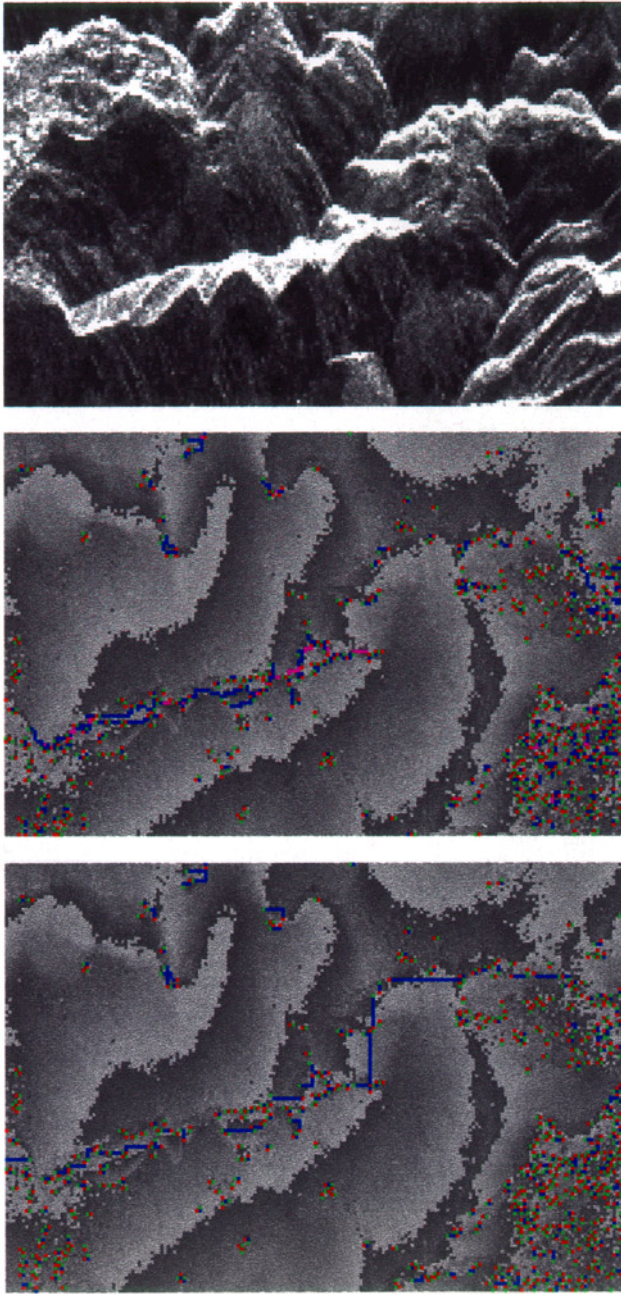


Figure 11. Wrapped phase (grey), residues (green, red), and branch-cuts (blue, multiple cuts: pink) found by a minimum cost flow algorithm. Left: minimization of total branch-cut length (constant costs); note the unrealistic long straight branch-cuts. Centre: minimization of a cost function derived from the phase gradient and its variance; the branch-cuts are guided along the ridges of the mountains (visible as bright areas in the intensity SAR image of the same area (right)).

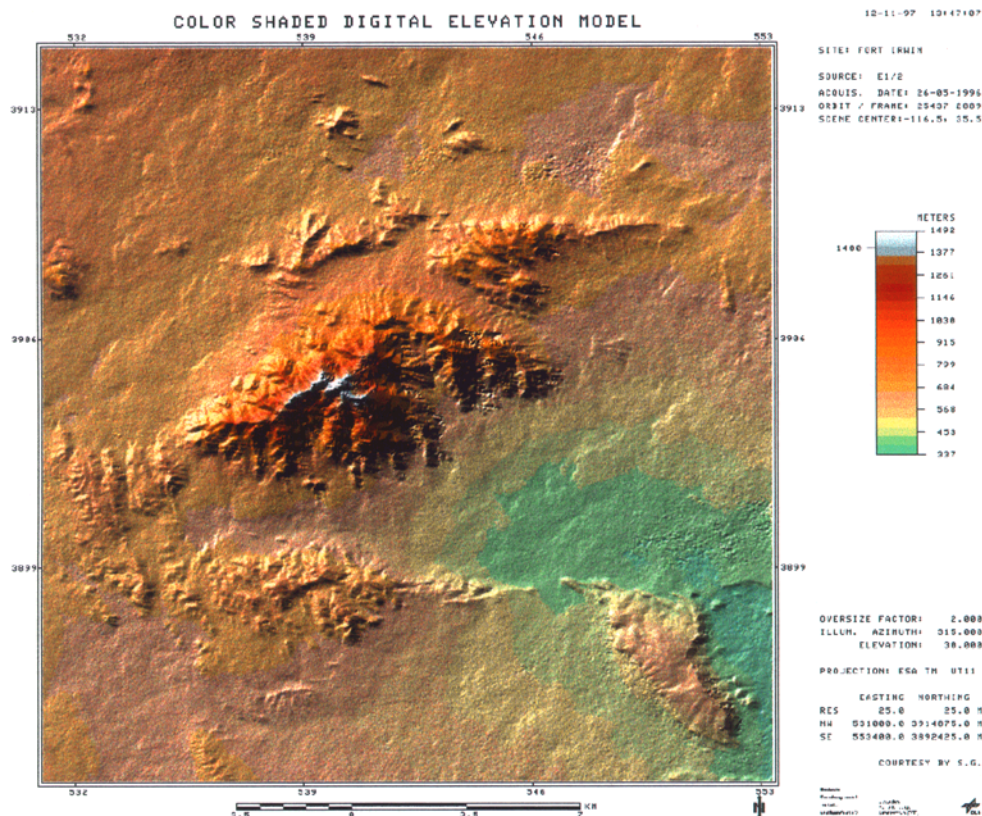


Figure 12. Digital elevation model generated from the ERS SAR interferograms of figures 8–10. Due to geo-referencing the DEM has a different orientation than the SAR data.

γ is the complex correlation coefficient (or *coherence*) of the two SAR images:

$$\gamma = \frac{E[u_1 u_2^*]}{\sqrt{E[|u_1|^2]E[|u_2|^2]}} = \frac{E[v]}{\bar{I}}. \quad (36)$$

Its phase is the expected interferometric phase ϕ_0 of the pixel under discussion; its magnitude is related to phase noise. Receiver noise, for example, may render the two images to be not fully correlated, i.e. $|\gamma| < 1$. Other more important causes of decorrelation will be discussed below.

The joint *pdf* of magnitude and phase of an interferogram sample $v = u_1 u_2^*$ can be shown to be (Lee *et al* 1994, Tough 1991)

$$pdf(|v|, \phi) = \frac{2|v|}{\pi \bar{I}^2 (1 - |\gamma|^2)} \exp \left\{ \frac{2|\gamma||v| \cos(\phi - \phi_0)}{\bar{I}(1 - |\gamma|^2)} \right\} K_0 \left(\frac{2|v|}{\bar{I}(1 - |\gamma|^2)} \right) \quad (37)$$

where $K_0(\cdot)$ is the modified Bessel function.

The marginal *pdf* of the interferometric *phase* can be derived from equation (37) (Davenport 1958, Goodman 1995, Just and Bamler 1994, Lee *et al* 1994, Middleton 1960, Sarabandi 1992, Tough 1991):

$$pdf(\phi) = \frac{1 - |\gamma|^2}{2\pi} \frac{1}{1 - |\gamma|^2 \cos^2(\phi - \phi_0)}$$

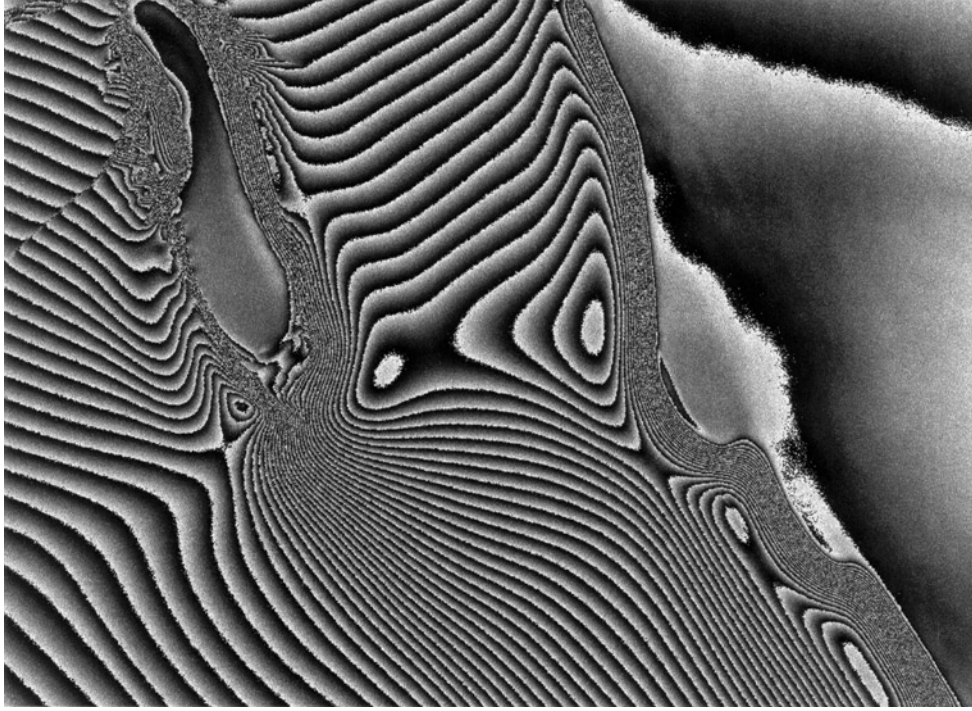


Figure 13. Surface movement measurement of the Hemmen Ice Rise (Filchner Ronne Shelf Ice, Antarctica) by D-InSAR (from Wu *et al* 1997). Interferometric phase (black: $-\pi$, white: $+\pi$) from two ERS-1 acquisitions ($\Delta t = 3$ days). The area is covered by snow and ice and is essentially flat. Hence, the phase is mainly due to (horizontal) shelf ice drift and to (vertical) tidal activity. Narrow fringe spacing indicates shear.

$$\times \left(1 + \frac{|\gamma| \cos(\phi - \phi_0) \arccos(-|\gamma| \cos(\phi - \phi_0))}{\sqrt{1 - |\gamma|^2 \cos^2(\phi - \phi_0)}} \right). \quad (38)$$

The *pdf* for the *interferogram magnitude* is

$$pdf(|v|) = \frac{4|v|}{\bar{I}^2(1 - |\gamma|^2)} I_0 \left(\frac{2|v||\gamma|}{\bar{I}(1 - |\gamma|^2)} \right) K_0 \left(\frac{2|v|}{\bar{I}(1 - |\gamma|^2)} \right). \quad (39)$$

The phase *pdf* is fully characterized by the two parameters ϕ_0 and $|\gamma|$. ϕ_0 is the desired (noise-free) phase used for topography reconstruction and $|\gamma|$ is a measure of phase noise. Of course, the support of any phase *pdf* is ambiguous. If we restrict phase values to an interval of width $\pm\pi$ centred at ϕ_0 then the mean and variance of the phase are (Tough 1991)

$$E[\phi] = \phi_0 \quad (40)$$

and

$$\sigma_\phi^2 = E[(\phi - \phi_0)^2] = \frac{\pi^2}{3} - \pi \arcsin(|\gamma|) + \arcsin^2(|\gamma|) - \frac{\text{Li}_2(|\gamma|^2)}{2} \quad (41)$$

where $\text{Li}_2(\cdot)$ is Euler's dilogarithm. Figure 22 shows the shape of the phase *pdf* for different coherence values. Obviously, the phase is uniformly distributed for $|\gamma| = 0$ and, hence, carries no information. When the coherence increases the phase distribution becomes

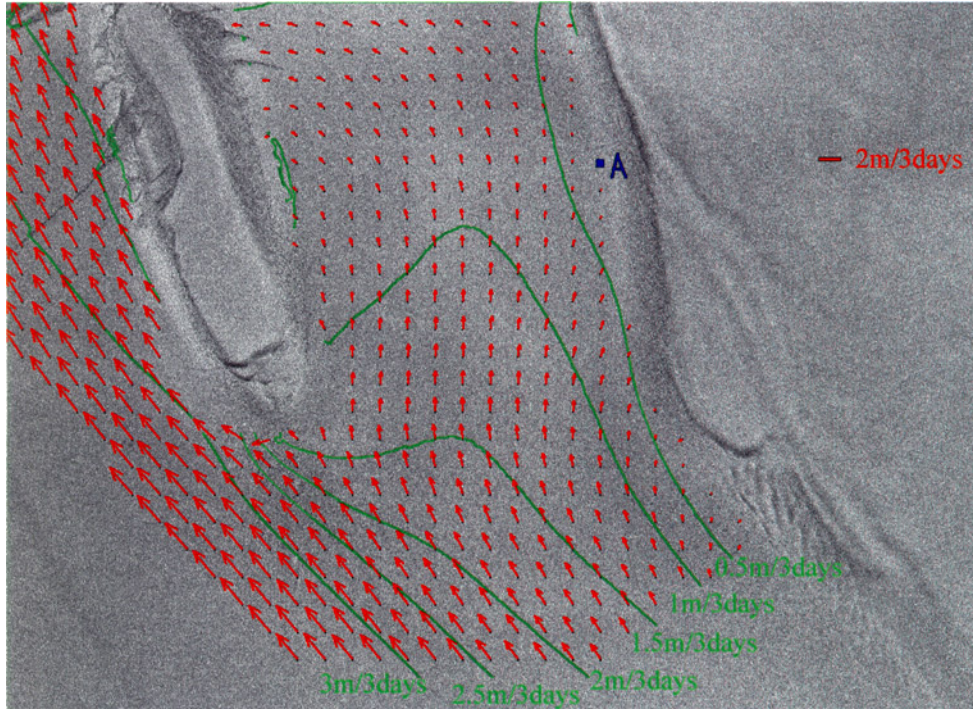


Figure 14. Surface movement measurement of the Hemmen Ice Rise (Filchner Ronne Shelf Ice, Antarctica) by D-InSAR (from Wu *et al* 1997). Estimated displacement vectors overlaid on SAR image. Vertical movements have been eliminated by using a tidal model. The vectors have been derived from two interferograms, one acquired from descending orbit (shown in figure 13) and a second one from ascending orbit. The orbits intersect at an angle of about 48° . Image size = $96 \text{ km} \times 56 \text{ km}$, data ©ESA.

more concentrated around its expectation value ϕ_0 , i.e. the phase noise variance decreases. In the limit of the noiseless case $|\gamma| = 1$ the *pdf* would degenerate to a δ -function.

3.6. Coherence

We have learnt from equations (33) and (41) that the statistics of interferograms of Gaussian scatterers are governed by the parameter *coherence* γ . Using equations (30) and (31) and the system model of figure 20 coherence can be expressed in terms of object and system properties (neglecting the leading constant phase term). Without loss of generality we may set $x = 0$ and $\eta = 0$ and obtain:

$$\gamma = \frac{\int \sigma_{ve}(\mathbf{r}) h_1(-x, -\eta) h_2^*(-x, -\eta) \exp\{-j2(\mathbf{k}_1 - \mathbf{k}_2) \cdot \mathbf{r}\} dV}{\sqrt{(S_1 + N_1)(S_2 + N_2)}} \quad (42)$$

where S_1 and S_2 are the noise-free signal intensities in the two SAR images (cf equation (16)):

$$S_1 = \int \sigma_{v1}(\mathbf{r}) |h_1(-x, -\eta)|^2 dV \quad \text{and} \quad S_2 = \int \sigma_{v2}(\mathbf{r}) |h_2(-x, -\eta)|^2 dV. \quad (43)$$



Figure 15. Crustal deformation caused by the 1995 Antofagasta (Chile) earthquake measured by D-InSAR (courtesy of Reigber *et al* 1997). Three ERS SAR data sets (one before and two after the earthquake) have been used to eliminate the topography induced phase. SAR image (magnitude). The lower left corner shows open sea.

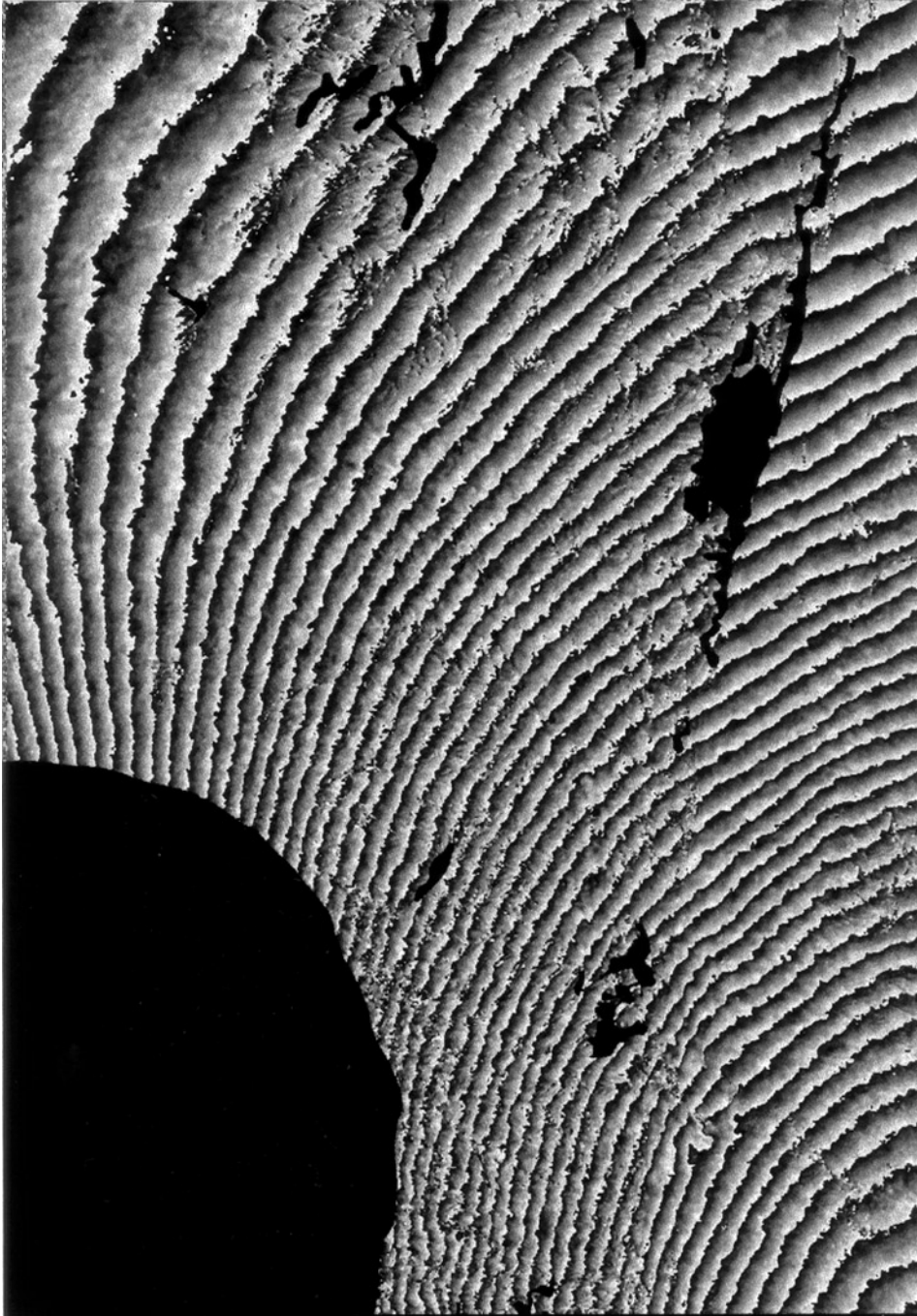


Figure 16. Phase caused by the seismic deformations (cf figure 15). The topographic phase has been removed by using a second interferogram where no displacement was present. One fringe cycle corresponds to a displacement of 0.9 cm in the slant range direction. Low coherence areas (water and lay-over) are masked out in black. The main reasons for these fringes are (1) a movement of the area from upper right to lower left and (2) an inflation with its maximum outside the lower right corner of the image. The displacements are in the range of tens of centimetres. Image size: about 40 km \times 55 km, data: ©ESA.

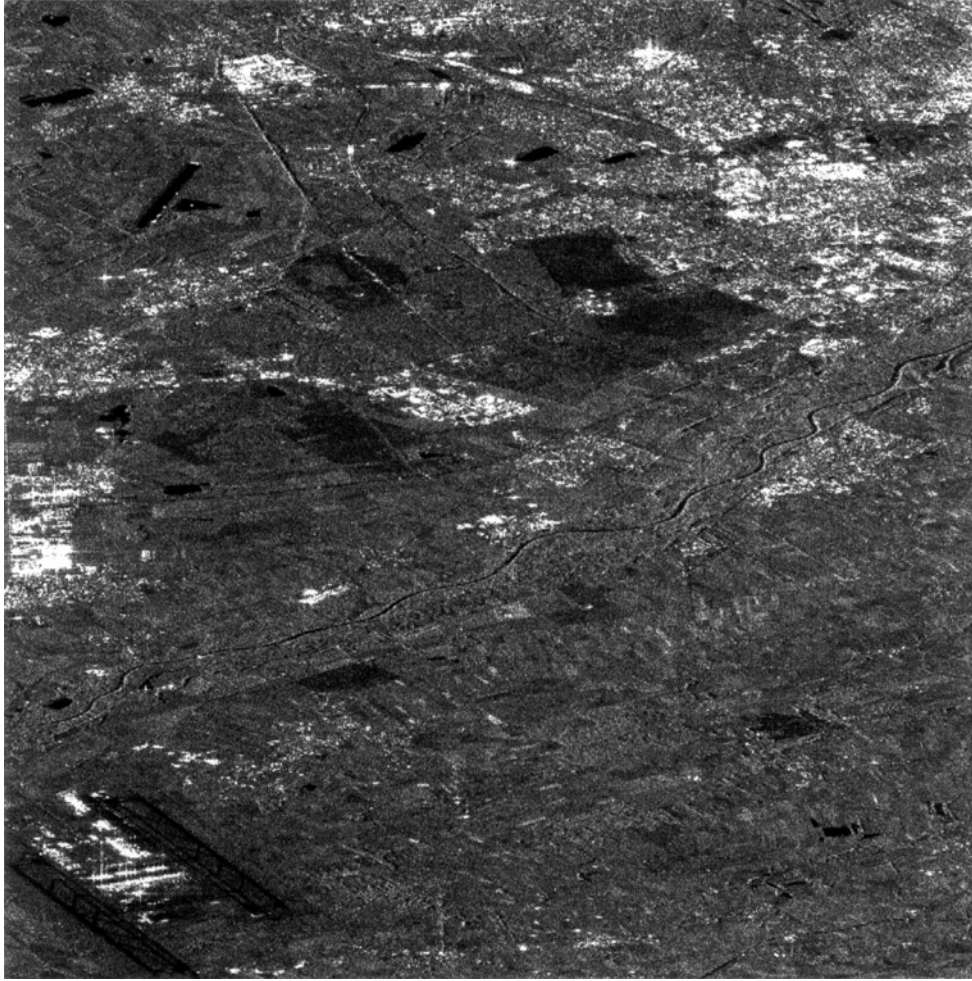


Figure 17. X-SAR intensity image.

Coherence can be written as the product of three dominant contributions (Rodriguez and Martin 1992, Zebker and Villasenor 1992):

$$\gamma = \gamma_{\text{SNR}} \gamma_H \gamma_a \quad (44)$$

which we shall now discuss. Each of these factors has a magnitude less than unity, i.e. it increases phase noise.

γ_{SNR} stands for the influence of finite *signal-to-noise ratio* (SNR) and can be readily factored out of equation (42) (Just and Bamler 1994, Zebker and Villasenor 1992):

$$\gamma_{\text{SNR}} = \frac{1}{\sqrt{(1 + N_1/S_1)(1 + N_1/S_2)}}. \quad (45)$$

γ_H describes the decorrelation caused by the fact that the two SAR signals have passed *different* filters $H_1(f_x, f_{\eta_1})$ and $H_2(f_x, f_{\eta_2})$. Seen from the 3D object spectrum point of view, those filters are inherently different, since they occupy different slices in the 3D spectral domain (cf figure 19). On top of that the 2D SAR system impulse response functions

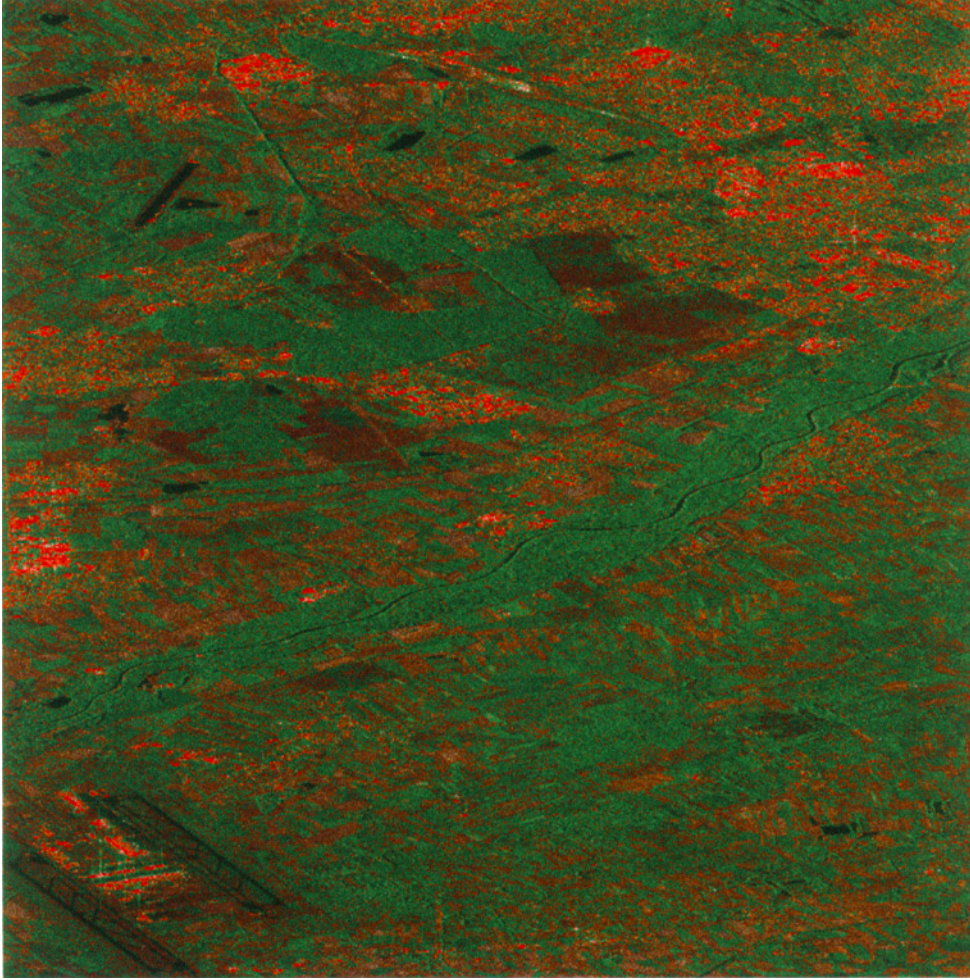


Figure 18. Intensity (grey value, cf figure 17) combined with coherence estimate (low coherence: green, high coherence: brown). Note the clear discrimination between different vegetation types (forest versus farmland); cities show up as bright and highly coherent features.

$h_1(x, \eta)$ and $h_2(x, \eta)$ may also be different due to the radar system or to processing (Just and Bamler 1994). Using equation (32) we can define γ_H as (Askne *et al* 1997, Ulander and Hagberg 1995)

$$\gamma_H = \frac{\int \sigma_{ve}(\mathbf{r}) h_1(-x, -\eta) h_2^*(-x, -\eta) \exp \left\{ -j2 \left(k \frac{B_{\perp}}{R_S} \zeta + \Delta k \eta \right) \right\} dV}{\sqrt{\int \sigma_{ve}(\mathbf{r}) |h_1(-x, -\eta)|^2 dV \int \sigma_{ve}(\mathbf{r}) |h_2(-x, -\eta)|^2 dV}}. \quad (46)$$

Given a certain class of scatterers and a particular imaging geometry (B_{\perp} , R_S etc) proper choices of a radar carrier frequency offset Δk and/or impulse response functions will be shown to be appropriate tools for coherence maximization.

γ_a stands for *temporal scene coherence* and is defined as the ratio of temporarily stable scattering contributions to the total scattering intensity transferred to the SAR images:

$$\gamma_a = \sqrt{\frac{\int \sigma_{ve}(\mathbf{r}) |h_1(-x, -\eta)|^2 dV \int \sigma_{ve}(\mathbf{r}) |h_2(-x, -\eta)|^2 dV}{\int \sigma_{v1}(\mathbf{r}) |h_1(-x, -\eta)|^2 dV \int \sigma_{v2}(\mathbf{r}) |h_2(-x, -\eta)|^2 dV}}. \quad (47)$$

If the two SAR images have been acquired at different times, the structure of the scatterer may have changed in the meantime. For example, water surfaces decorrelate within tens of milliseconds and will show no coherence at all in a repeat-pass interferogram. Forests tend to decorrelate due to movement of leaves and branches; their coherence is typically in the order of 0.2 in C-band repeat-pass interferograms. Of course, manmade changes such as ploughing of an agricultural area completely destroy coherence.

Hence, γ_a is an important property of the imaged object. We will show later that scene coherence can be used for classification of different types of scatterers.

3.7. Surface scattering

In the case of pure surface scattering we have, e.g.

$$\sigma_{ve}(\mathbf{r}) = \sigma_e^0(x, y) \delta(z) = \sigma_e^0(x, y) \delta(-\eta \cos \theta + \zeta \sin \theta). \quad (48)$$

Inserting into equation (46) and assuming that $\sigma_e^0(x, y)$ is quasistationary we find

$$\gamma_{H,\text{surface}} = \frac{\int h_1(x, \eta) h_2^*(x, \eta) \exp \left\{ -j2 \left(\frac{k B_\perp}{R_S \tan \theta} + \Delta k \right) \eta \right\} dx d\eta}{\sqrt{\int |h_1(x, \eta)|^2 dx d\eta \int |h_2(x, \eta)|^2 dx d\eta}}. \quad (49)$$

(If the scattering surface is tilted towards the SAR by a terrain slope of α , θ must be replaced by $\theta - \alpha$.) Obviously, the different look angles of the two SAR images, i.e. $B_\perp \neq 0$, have the effect of decorrelating the signals. The physical reason is that the coherent sum of contributions from the individual scatterers within a resolution element on ground varies with aspect angle.

3.8. Spectral shift

The geometric decorrelation effect can, for example, be avoided by using SARs of slightly different frequencies (Gatelli *et al* 1994) with

$$\Delta k = -\frac{k B_\perp}{R_S \tan(\theta - \alpha)} \quad (50)$$

because in that case the exponent in equation (49) vanishes. Since in most SAR systems the radar frequency is constant ($\Delta k = 0$) by design, the processing filters must be tuned to different centre frequencies, a procedure known as wavenumber (or spectral) shift filtering (Gatelli *et al* 1994):

$$h_2(x, \eta) = h_1(x, \eta) \exp\{-j2\pi \Delta f_R \eta\} \quad (51)$$

where

$$\Delta f_R = \frac{2B_\perp}{\lambda R_S \tan(\theta - \alpha)}. \quad (52)$$

The amount of spectral shift is identical to the local fringe frequency in range f_ϕ (cf equation (29)). Thus we can write equation (49) in a compact form both in space and in

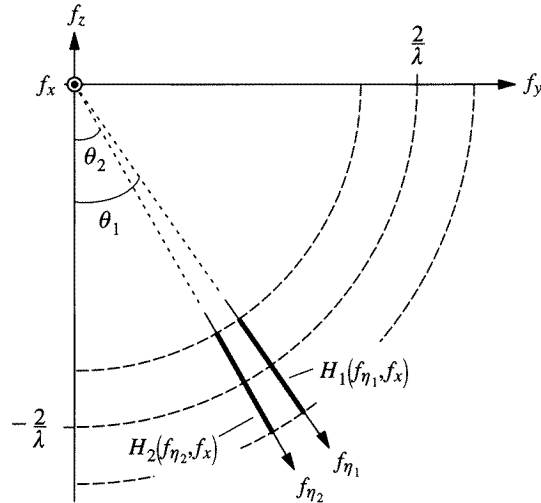


Figure 19. Slices (bold) of the object spectrum that contribute to an across-track interferogram.

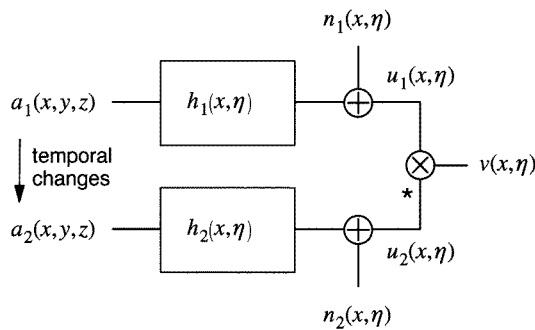


Figure 20. Linear system theoretical model of SAR interferometry.

frequency domain (for $\Delta k = 0$):

$$\begin{aligned} \gamma_{H, \text{surface}} &= \frac{\int h_1(x, \eta) h_2^*(x, \eta) \exp\{-j2\pi f_\phi \eta\} dx d\eta}{\sqrt{\int |h_1(x, \eta)|^2 dx d\eta \int |h_2(x, \eta)|^2 dx d\eta}} \\ &= \frac{\int H_1(f_x, f_\eta) H_2^*(f_x, f_\eta - f_\phi) df_x df_\eta}{\sqrt{\int |H_1(f_x, f_\eta)|^2 df_x df_\eta \int |H_2(f_x, f_\eta)|^2 df_x df_\eta}}. \end{aligned} \quad (53)$$

This version is especially helpful for analysing the influence of processor aberrations on interferogram coherence (Just and Bamler 1994).

A geometric interpretation of spectral shift is given in figure 23. Every ground range frequency component is mapped into a SAR signal frequency according to the sine of the local incidence angle which is slightly different for the two images. Hence, the SAR system of wavenumber k and range signal bandwidth W_R ‘sees’ different ground range frequency components in the two acquisitions. Only the common ground frequency band carries interferometric information, the non-common spectral components may be used to increase ground range resolution beyond the limit of the single SAR system (figure 24) (Gatelli *et al* 1994, Prati and Rocca 1993). Another illustration of spectral shift is obtained

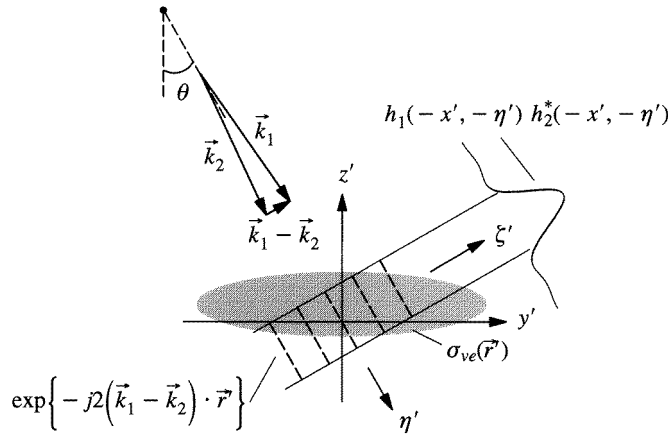


Figure 21. Illustration of equations (31) and (32). $|k_1| = |k_2|$ is assumed.

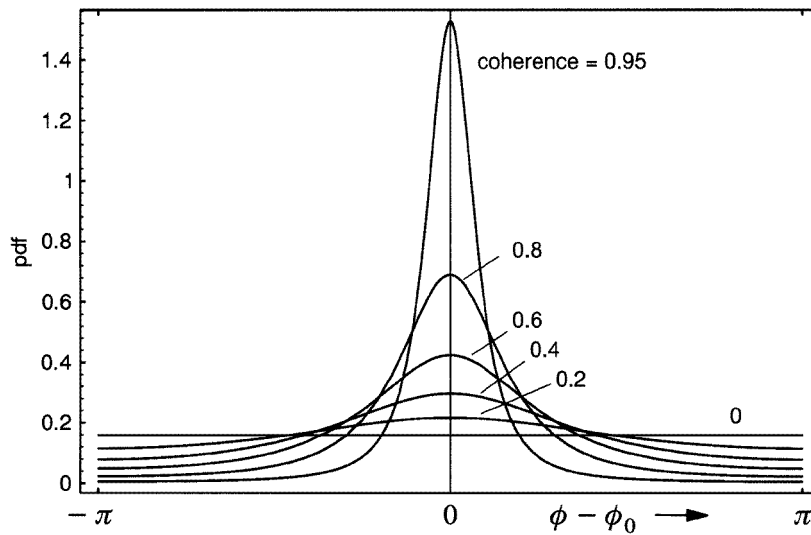


Figure 22. Probability density functions of the interferometric phase for different values of coherence.

from figure 19. Considering that the spectrum of a surface scatterer is constant in the f_z direction it becomes obvious that $H_1(\cdot)$ and $H_2(\cdot)$ cover different, though overlapping, f_z support.

Without spectral shift filtering coherence drops as a function of baseline like the cross-correlation function of the transfer functions. Spectral shift filtering attempts to make $H_1(f_x, f_\eta) = H_2(f_x, f_\eta - f_\phi)$ and, hence, $\gamma_{H, \text{surface}} = 1$. For rectangular transfer functions this means chopping off a frequency band of width $\Delta f_R = f_\phi$ both from the high-frequency edge of $H_1(\cdot, \cdot)$ and from the low-frequency edge of $H_2(\cdot, \cdot)$. In practice this requires knowledge of the local fringe frequency f_ϕ , which is a function of local terrain slope. Therefore, optimum slope-adaptive spectral shift filtering can improve interferogram quality (Bamler and Davidson 1997).

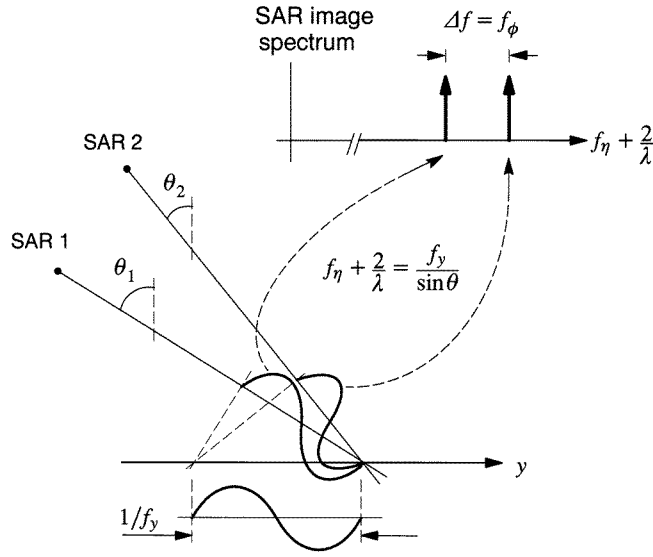


Figure 23. Geometric interpretation of spectral shift.

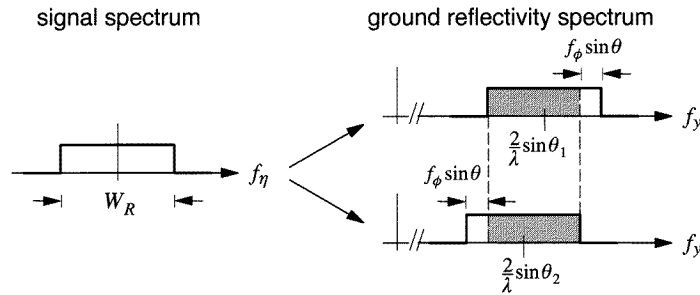


Figure 24. Mapping of SAR system bandwidth to ground range frequencies. The common spectral band used for interferometry is shaded.

The maximum allowable spectral shift is the system bandwidth W_R which limits the baseline to values smaller than the so-called *critical baseline*:

$$B_{\perp, \text{crit}} = \frac{\lambda(W_R + \Delta k/\pi)R_S \tan(\theta - \alpha)}{2}. \quad (54)$$

For example $B_{\perp, \text{crit}} \cong 1.1$ km for ERS-1/2 ($\Delta k = 0$) and flat terrain ($\alpha = 0$). Given a rectangular system transfer function the baseline dependence of γ_H without spectral shift filtering can be expressed as

$$|\gamma_H| = 1 - \frac{B_{\perp}}{B_{\perp, \text{crit}}} \quad \text{for } B_{\perp} \leq B_{\perp, \text{crit}}. \quad (55)$$

It is interesting to have a closer look at spectral shift as a function of terrain slope α . Figure 25 depicts this relationship for the full range of slope angles (ERS case). At grazing incidence, i.e. $\alpha = \theta - 90^\circ$, $f_\eta + 2/\lambda \cong f_y$ for both images and the spectral shift is zero. This is the transition to radar shadow. Spectral shift increases with terrain slope to the point where it equals the range system bandwidth. At larger slopes no common spectral bands are available for interferometric use. Beyond $\alpha = \theta$ lay-over causes range-reversed imaging

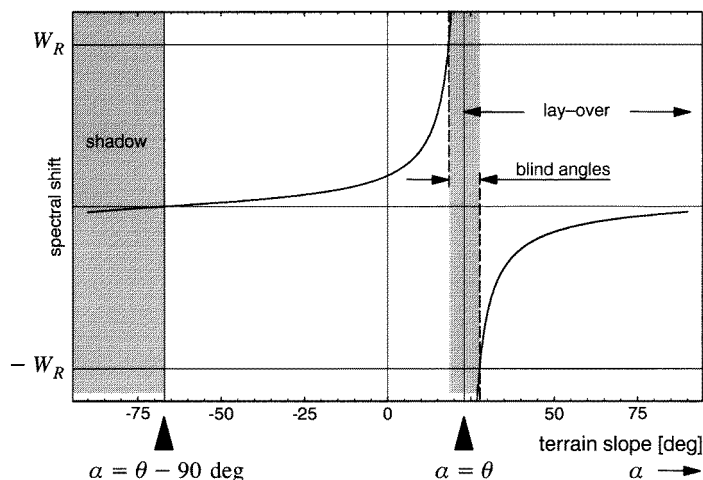


Figure 25. Spectral shift f_ϕ as a function of terrain slope; ERS system parameters ($\theta = 23^\circ$) and 200 m baseline are assumed.

and spectral shift is negative. Knowing this, lay-over can be separated from non-lay-over by range filtering the interferogram for negative and positive fringe frequencies, respectively (Gatelli *et al* 1994). No information, however, can be extracted for shadow areas and for slopes in the blind angle interval as marked in figure 25.

3.9. Volume scattering

In order to illustrate the influence of volume scattering on coherence (cf equation (46)) it is useful to focus on scatterers whose backscatter coefficient can be characterized as a profile in z and is constant in x and y :

$$\sigma_{ve}(\mathbf{r}) = p(z). \quad (56)$$

Then equation (46) can be rewritten in a convenient form as follows

$$\gamma_H = \frac{P\left(\frac{f_\phi}{\cos\theta}\right) S\left(f_\phi + \frac{\Delta k}{\pi} - 2\Delta f_R\right)}{P(0)S(0)} \quad (57)$$

where $P(\cdot)$ and $S(\cdot)$ are the Fourier transforms of $p(z)$ and $|h(\eta)|^2$, respectively. Hence, $S(\cdot)$ is the autocorrelation function of the transfer function $H(f_\eta)$. (For the sake of compactness we have suppressed the azimuth dependence here.) f_ϕ is the local range fringe frequency of equation (29); it is proportional to the baseline.

Obviously, γ_H is a product of a contribution known from surface scattering ($S(\cdot)/S(0)$) and the volume decorrelation factor $P(\cdot)/P(0)$. Both depend on the baseline; the surface scattering term demands for spectral shift filtering as described above. In the case of pure surface scattering we have $p(z) = \delta(z)$ and $P(f_z) = 1$. Then equation (57) degenerates to equation (53).

3.10. Estimation of interferometric phase

The phase ϕ of an interferogram pixel is the primary quantity used, for example, for terrain reconstruction. We have seen that the phase must be considered as a random variable and,

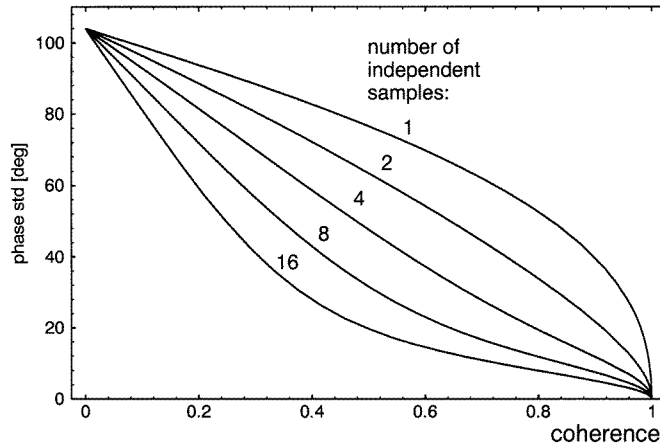


Figure 26. Standard deviation of the phase estimate as a function of coherence and number of independent samples L .

hence, phase determination is an estimation problem. The first-order statistics of a sample phase value are described by equations (38) and (40). Often phase estimates will be based on more than one interferogram sample each. Rather, several interferogram values in a small estimation window will be used or several independent interferograms of lower resolution are computed by dividing the available SAR system bandwidth into several narrower bands (so-called ‘looks’).

In either case let us assume that we want to estimate the phase from L independent interferogram samples $v[n]$. Provided that the expected phase originating from terrain and interferometer geometry is constant for all these samples, the *maximum likelihood estimator* (MLE) for phase is

$$\hat{\phi}_{\text{MLE}} = \arg \left\{ \sum_{n=1}^L v[n] \right\}. \quad (58)$$

The probability density of this phase estimate becomes (Joughin *et al* 1994, Lee *et al* 1994, Touzi and Lopes 1996)

$$\begin{aligned} pdf(\hat{\phi}; L) = & \frac{\Gamma(L + 1/2)(1 - |\gamma|^2)^L |\gamma| \cos(\phi - \phi_0)}{2\sqrt{\pi}\Gamma(L)(1 - |\gamma|^2 \cos^2(\phi - \phi_0))^{L+1/2}} \\ & + \frac{(1 - |\gamma|^2)^L}{2\pi} {}_2F_1(L, 1; \frac{1}{2}; |\gamma|^2 \cos^2(\phi - \phi_0)) \end{aligned} \quad (59)$$

where ${}_2F_1$ is the hypergeometric function.

Figure 26 shows the phase noise standard deviation as a function of coherence and number of looks. It is interesting to note that (for high coherence) averaging of L independent complex interferogram samples reduces phase noise by more than the $1/\sqrt{L}$ -law (as would be expected if independent phase values were averaged). The reason lies in the interdependence of interferogram phase and magnitude. Examining equation (37) more closely it becomes evident that those interferogram samples whose phase is close to ϕ_0 are more likely to have high amplitude, while higher phase deviations more often come with small amplitudes.

For some applications not only the phase is of interest but also its local gradient, i.e. the local fringe frequency f_ϕ (possibly both its range and azimuth components). Assuming

that the topography-induced phase varies linearly in range and azimuth within an estimation window, the *MLE of fringe frequency* is simply found via Fourier transform and searching for the frequency component of highest magnitude.

3.11. Estimation of coherence

Coherence is another quantity to be estimated. First, it is a measure for local interferogram quality and is thus needed in many interferometric signal processing steps. Secondly it provides valuable information about the scatterer; for example in repeat-pass interferometry temporal decorrelation is often exploited for object classification (Askne and Smith 1996, Borgeaud and Wegmüller 1996, Floury *et al* 1997, 1996, Wegmüller and Werner 1997); in single-pass configurations coherence can give rough estimates of the thickness of the scattering layer (canopy thickness, penetration depth, etc) according to equation (57).

Assuming that we want to estimate the magnitude of coherence from L independent samples of u_1 and u_2 each, the MLE is found by replacing expectation values by averages:

$$|\hat{\gamma}|_{\text{MLE}} = \frac{\left| \sum_{n=1}^L u_1[n] u_2^*[n] \right|}{\sqrt{\sum_{n=1}^L |u_1[n]|^2 \sum_{n=1}^L |u_2[n]|^2}}. \quad (60)$$

The probability density of this estimate has been shown to be (Touzi and Lopes 1996, Touzi *et al* 1997)

$$pdf(|\hat{\gamma}|; L) = 2(L-1)(1-|\gamma|^2)^L |\hat{\gamma}| (1-|\hat{\gamma}|^2)^{L-2} {}_2F_1(L, L; 1; |\gamma|^2 |\hat{\gamma}|^2). \quad (61)$$

The mean and the moments of order k are, respectively:

$$E[|\hat{\gamma}|] = \frac{\Gamma(L)\Gamma(1+k/2)}{\Gamma(L+k/2)} {}_3F_2\left(\frac{3}{2}, L, L; L+\frac{1}{2}; 1; |\gamma|^2\right) (1-|\gamma|^2)^L \quad (62)$$

and

$$E[|\hat{\gamma}|^k] = \frac{\Gamma(L)\Gamma(1+k/2)}{\Gamma(L+k/2)} {}_3F_2\left(1+k/2, L, L; L+k/2; 1; |\gamma|^2\right) (1-|\gamma|^2)^L. \quad (63)$$

Unfortunately, this estimate is *biased* (Joughin *et al* 1994, Touzi and Lopes 1996, Touzi *et al* 1997); it tends to overestimate low coherence, i.e. $E[|\hat{\gamma}|] \geq |\gamma|$. For large numbers of samples L it becomes asymptotically unbiased. Figure 27 shows $E[|\hat{\gamma}|]$ as a function of the ‘true’ coherence and the number of samples. For approaches toward unbiased coherence estimation see Touzi *et al* (1997).

In many quick-and-dirty calculations the variance of the coherence estimate is required without going into tedious evaluations of equation (63). Then the Cramér–Rao bound for unbiased coherence estimation is often used:

$$\text{var}(|\hat{\gamma}|)_{\text{CR}} = \frac{(1-|\gamma|^2)^2}{2L}. \quad (64)$$

Figure 28 compares the standard deviation of the MLE with the Cramér–Rao bound. The latter one is in good agreement with the MLE for high coherence and high number of samples. For low coherence the MLE performs better than the Cramér–Rao bound which is only applicable as a lower limit for *unbiased* estimators.

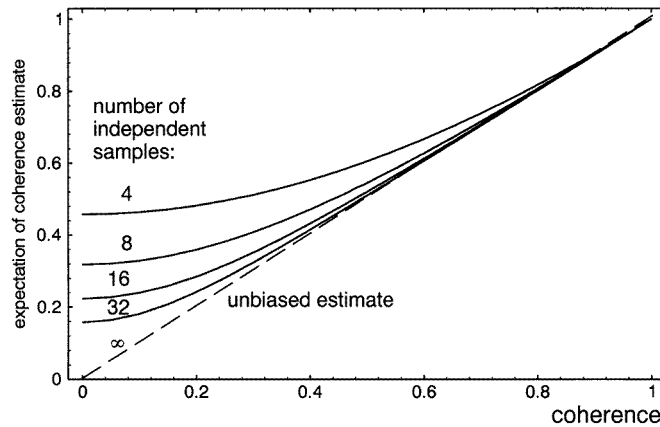


Figure 27. Bias of the MLE coherence estimator.

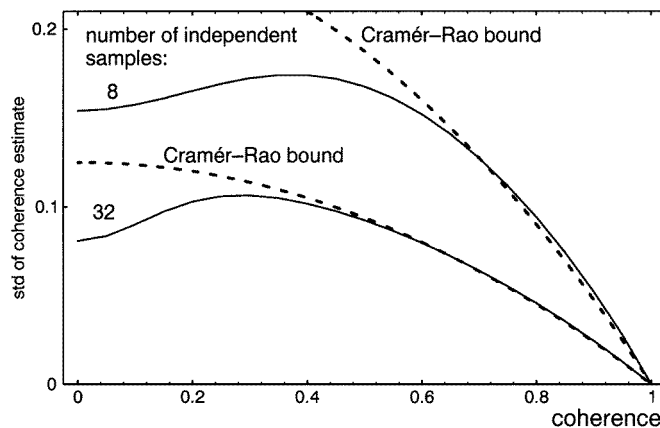


Figure 28. Standard deviation of the (biased) coherence MLE compared with the Cramér-Rao bound for unbiased estimates.

4. Phase unwrapping

We have seen how to estimate the phase ϕ from interferogram samples. Phase estimates, however, are still ambiguous by integer multiples of 2π . For applications such as terrain reconstruction from across-track interferograms we must resolve this ambiguity.

Terrain height is (roughly) proportional to a (non-ambiguous!) range difference. Let us denote the *topography-induced phase* by

$$\phi_T = 2k\Delta R. \quad (65)$$

It is the quantity we want to estimate at the end. Due to decorrelation effects discussed above interferometric phase is disturbed by noise. Accepting the agreement from section 3 that the support of the *pdf* of ϕ (equations (38) and (59)) be centred at its expectation value we may consider the phase noise ϕ_N as *additive*:

$$\phi = \phi_T + \phi_N \quad \text{where } E[\phi] = \phi_T \text{ and } \phi_N \in [-\pi, \pi). \quad (66)$$

If the *absolute phase* ϕ could be measured unambiguously, well known reconstruction methods for signal in additive noise could be applied to obtain an estimate of ϕ_T according

to some optimality criterion.

The observable interferogram phase can be any value $\phi + n2\pi$, where n is an integer. Without loss of generality we may restrict the interferogram phase to the principal interval $[-\pi, \pi)$. Let us define the operator $W\{\cdot\}$, that wraps ϕ into that interval and outputs the *wrapped phase* ψ :

$$\psi = W\{\phi\} = \text{mod}\{\phi + \pi, 2\pi\} - \pi \quad \in [-\pi, \pi). \quad (67)$$

The aim of phase unwrapping can be stated as follows. Find an estimate $\hat{\phi}$ of the ‘true’ phase ϕ given its principle (wrapped) value ψ . To solve this problem, additional information/assumptions must be employed.

Let the 2D phase maps under discussion be functions of discrete coordinates i and k . Further define discrete equivalents to partial derivatives of a function F as

$$\begin{aligned} \Delta_i F(i, k) &= F(i + 1, k) - F(i, k) \\ \Delta_k F(i, k) &= F(i, k + 1) - F(i, k) \end{aligned} \quad (68)$$

and compact them into *gradient* notation:

$$\nabla F(i, k) = \begin{pmatrix} \Delta_i F(i, k) \\ \Delta_k F(i, k) \end{pmatrix}. \quad (69)$$

We will also use the discrete version of the *curl* of a 2D vector field $\mathbf{A} = (A_i, A_k)^T$, which is a scalar field:

$$\begin{aligned} \nabla \times \mathbf{A}(i, k) &= \Delta_i A_k(i, k) - \Delta_k A_i(i, k) \\ &= A_k(i + 1, k) - A_k(i, k) - A_i(i, k + 1) + A_i(i, k). \end{aligned} \quad (70)$$

It is equivalent to the enclosure integral in the 2×2 neighbourhood of the pixel (i, k) . As is known from vector analysis the curl of a gradient field—or any *conservative* field—is zero everywhere, i.e. $\nabla \times \nabla F = 0$.

Returning to the problem of estimating $\phi(i, k)$ from $\psi(i, k)$ it is clear that we have to include some prior knowledge about the phase—or the terrain—to be reconstructed. Otherwise we would have no indication that $\psi(i, k)$ itself is not the correct phase. The high phase discontinuities of up to $\pm 2\pi$ inherent in $\psi(i, k)$ are not very likely to be caused by natural terrain. Hence, the *phase gradient* seems to be the quantity where disturbing contributions from the wrapping operator of equation (67) can possibly be separated from true phase. This heuristic and intuitive argument leads to the following two-step paradigm underlying almost all current phase unwrapping algorithms.

First, an *estimate* $\hat{\nabla}\psi$ of the *phase gradient* plus some reliability measure of the estimate is obtained from the wrapped phase ψ or from the complex interferogram samples. Secondly, this estimate is integrated either via a one-dimensional (1D) summation or by a 2D convolution where weighting according to the reliability of gradient estimates may be optionally employed. Different phase unwrapping algorithms differ in the way these two steps are performed. For a comparison of phase unwrapping methods see also Ghiglia and Pritt (1998).

4.1. Gradient estimate

Being an estimate, $\hat{\nabla}\psi$ will always be subject to errors \mathbf{n}_∇ ,

$$\hat{\nabla}\psi(i, k) = \nabla\psi(i, k) + \mathbf{n}_\nabla(i, k) \quad (71)$$

which render the phase gradient estimate in general *non-conservative*:

$$\nabla \times \hat{\nabla}\psi(i, k) = \nabla \times \mathbf{n}_\nabla(i, k) \neq 0. \quad (72)$$

Hence, an integration of $\hat{\nabla}\psi$ will be path dependent.

Most of the phase unwrapping algorithms start from the assumption that in a properly sampled interferogram the phase differences of adjacent samples are likely to be $\in [-\pi, \pi)$. This leads to the popular *wrapped-differences-of-wrapped-phases* estimator:

$$\hat{\nabla}\psi(i, k) = \begin{pmatrix} W\{\Delta_i\psi(i, k)\} \\ W\{\Delta_k\psi(i, k)\} \end{pmatrix} \quad (73)$$

i.e. the phase gradient is estimated by computing partial derivatives of $\psi(i, k)$ and—in the case where they exceed $\pm\pi$ —wrapping them back to their more likely values in the principal interval. Obviously, the error $\mathbf{n}_{\nabla}(i, k)$ is either zero if $|\Delta_i\phi(i, k)| < \pi$ and $|\Delta_k\phi(i, k)| < \pi$ (which is true for most of the pixels) or consists of isolated vectors whose components are non-zero integer multiples of 2π whenever the true phase differences exceed $\pm\pi$. Two mechanisms are responsible for phase differences exceeding $\pm\pi$ and, hence, the occurrence of local $\mathbf{n}_{\nabla}(i, k)$ -vectors; these are terrain undersampling and noise.

(1) In rugged terrain, slopes may be arbitrarily steep and lead to high phase derivatives if not to lay-over. These topography-induced errors cause interferometric fringes to merge or end ‘mysteriously’.

(2) Even in the absence of terrain, undersampling phase derivatives larger than $\pm\pi$ may occur. Consider an absolutely flat topographic phase, e.g. $\phi_T(i, k) = \phi_0$ and a coherence $\gamma < 1$. The phase *pdf* of an interferogram sample is shown in figure 22. Its support is $[\phi_0 - \pi, \phi_0 + \pi)$. The *pdf* of the phase difference between two (independent) samples is the autocorrelation of the phase *pdf* and, hence, has twice the support, i.e. $[-2\pi, 2\pi)$. The lower the coherence the more likely derivatives exceeding $\pm\pi$ are.

4.2. Slope bias

$\mathbf{n}_{\nabla}(i, k)$ has some unconventional properties (Bamler *et al* 1998, 1996a, Spagnolini 1993). Its relationship to the true phase is highly nonlinear due to the wrapping operator involved. It is *not independent* of $\nabla\phi(i, k)$ as one would expect from equation (71). To illustrate this, consider a linear phase ramp of gradient \mathbf{G} :

$$\phi_T(i, k) = \phi_0 + iG_i + kG_k. \quad (74)$$

Due to the additive phase noise assumption of equation (66) we have

$$E[\nabla\phi(i, k)] = \mathbf{G}. \quad (75)$$

For the phase gradient estimate $\hat{\nabla}\psi$ to be unbiased, $E[\mathbf{n}_{\nabla}(i, k)]$ must be zero. To show that this is not true we focus on the i -components of the involved vectors for a moment. Further we take $0 < G_i < \pi$. The i -component of $E[\mathbf{n}_{\nabla}(i, k)]$ is

$$E[W\{\Delta_i\psi(i, k)\} - \Delta_i\phi(i, k)] = E[W\{G_i + \Delta_i\phi_N\}] - G_i. \quad (76)$$

Per definition,

$$W\{G_i + \Delta_i\phi_N\} - G_i = \begin{cases} 2\pi & \Delta_i\phi_N < -\pi - G_i \\ 0 & -\pi - G_i \leq \Delta_i\phi_N < \pi - G_i \\ -2\pi & \pi - G_i \leq \Delta_i\phi_N \end{cases} \quad (77)$$

where the *pdf* of $\Delta_i\phi_N$ is again the autocorrelation function of the one depicted in figure 22. It is symmetric with support $[-2\pi, 2\pi)$. Hence, for a positive gradient it is more likely for an error of -2π to occur than one of $+2\pi$. As a consequence, the gradient estimation error is *non-zero-mean* and depends on terrain slope and coherence. It has a net component pointing ‘down the slope’:

$$E[\mathbf{n}_{\nabla}(i, k)] \neq 0 \uparrow\downarrow \mathbf{G}. \quad (78)$$

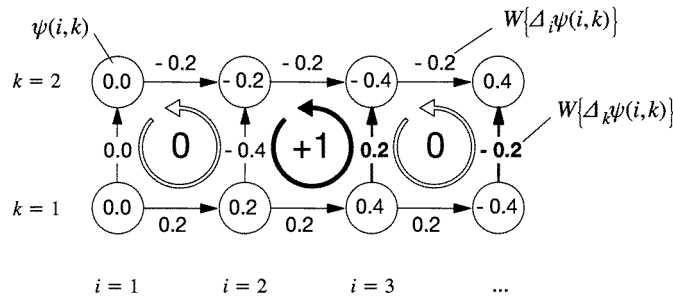


Figure 29. Example of a topography-induced residue (phases and residue charges are given in cycles, i.e. multiples of 2π). The topographic phase exhibits a shear between a negative slope of $-0.2/\text{sample}$ at row $k = 2$ and a positive slope of $0.2/\text{sample}$ at $k = 1$. At $i \geq 3$ the true phase difference between upper and lower row exceeds 0.5 cycles and the phase gradient estimate $W\{\Delta_k \psi\}$ is wrong by 1 cycle (bold). This is indicated by a positive residue.

Its magnitude increases with slope and decreases with coherence. Any phase unwrapping algorithm that does not take this special nature of $n_{\nabla}(i, k)$ into account will *underestimate* slopes and distort the reconstructed terrain. In particular this is true for all *linear* methods such as unweighted least squares estimation.

The problem of slope bias in the phase gradient estimate can be partially avoided if $\hat{\nabla}\psi$ is estimated on a larger window rather than on three samples only (as suggested by equation (73)). In fact, phase gradient is equivalent to local fringe frequency and many known frequency estimators may be applied as well (Spagnolini 1995). These methods may operate on the complex interferogram samples rather than on their phase only. The larger the estimation window, and, hence, the lower the spatial resolution, the lower is the probability of wrapping errors (aliasing). This requires a trade-off between estimation accuracy and resolution taking the local interferogram quality (coherence) into account. Multiresolution frequency analysis allows for such an adaptive adjustment of window sizes. A fast hierarchical implementation of a multiresolution estimator has been shown to provide asymptotically unbiased gradient estimates (Bamler and Davidson 1997, Davidson and Bamler 1996, 1998).

4.3. Residues

The phase gradient estimate of equation (73) has the advantage that its errors are local and come in integer multiples of 2π . The fact that according to equation (72) $n_{\nabla}(i, k)$ carries the solenoidal part of the phase gradient estimate field can be used to identify these errors. Let us refer to the curl of $\hat{\nabla}\psi(i, k)$ as the *residue field* (Goldstein *et al* 1988):

$$\begin{aligned} r(i, k) &= \nabla \times \hat{\nabla}\psi(i, k) = \nabla \times n_{\nabla}(i, k) \\ &= W\{\Delta_i \psi(i, k)\} + W\{\Delta_k \psi(i + 1, k)\} - W\{\Delta_i \psi(i, k + 1)\} - W\{\Delta_k \psi(i, k)\}. \end{aligned} \quad (79)$$

Its values are either zero (no residues) or $\pm 2\pi$ (positive or negative residue, respectively). Figure 29 shows how the location of a residue is related to phase gradient estimation errors.

Residues obviously mark the endpoints of lines in the interferogram along which the true phase gradient exceeds $\pm\pi/\text{sample}$. These lines are often referred to as ‘branch-cuts’ or ‘ghost lines’. As mentioned above, high gradients may either be caused by steep terrain slopes or by decorrelation phase noise. In the first case the branch-cuts follow the terrain

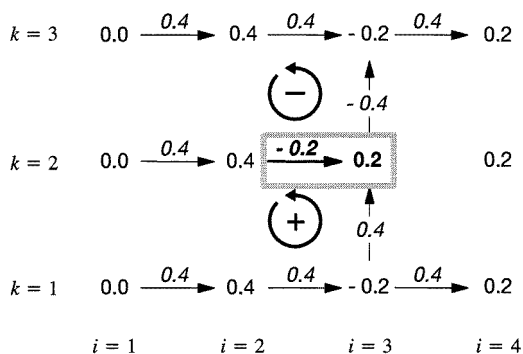


Figure 30. Example of a noise-induced residue dipole (phases and residue charges are given in cycles, i.e. multiples of 2π). The noise-free phase is assumed to be a ramp of slope 0.4/sample in the i -direction. Due to decorrelation noise the (wrapped) phase value at $(i, k) = (3, 2)$ was perturbed from its true value of -0.2 to 0.2 . As a result the phase difference between samples $(i, k) = (2, 2)$ and $(i, k) = (3, 2)$ becomes 0.8 and, thus, gets wrapped to the value -0.2 . This aliased gradient generates a positive and a negative residue in the adjacent cells. The connecting line of the residues marks the wrong difference estimate.

discontinuity and may extend over many samples, while in the latter case often only single phase gradient estimates are off by $\pm 2\pi$, i.e. branch-cuts are only one sample long. In either case every branch-cut carries one positive and one negative residue at its endpoints. Figure 30 shows how a single error in the phase gradient estimate generates such a residue ‘dipole’.

The residue density in an interferogram, i.e. the number of residues per sample, increases with phase noise. The maximum density is reached for totally decorrelated data ($\gamma = 0$) and can be shown to be $\frac{1}{3}$ (Gatelli *et al* 1994).

4.4. Branch-cut phase unwrapping methods

From the mentioned arguments it should be obvious that when integrating the phase gradient estimate $\hat{\nabla}\psi(i, k)$ one must avoid crossing a branch-cut (where $\hat{\nabla}\psi(i, k)$ is wrong). Branch-cut based phase unwrapping methods attempt to identify these lines and either exclude them from the integration path (Goldstein *et al* 1988) or use them to correct the phase difference estimates along the branch-cut by adding integer multiples of 2π /sample before (unrestricted) integration (Costantini 1996, 1998, Flynn 1997). A welcome property of these methods is that the unwrapped phase $\hat{\phi}(i, k)$ is consistent (or congruent (Pritt 1997)) with the wrapped phase, i.e. they differ only by integer multiples of 2π :

$$W\{\hat{\phi}(i, k)\} = W\{\phi(i, k)\} = \psi(i, k). \quad (80)$$

Within this framework, the art of phase unwrapping consists of finding the branch-cuts, or, in other words, an estimate of the phase gradient error $n_{\nabla}(i, k)$ from equation (71). In the case of an isolated noise-induced residue dipole like the one in figure 30 this task is simple. However, as the residue density increases it may no longer be possible to identify residue dipoles unambiguously without employing additional information. Also in the case of topography-induced residues the branch-cuts will in general be several samples long and their location is ambiguous. Wrongly guided branch-cuts result in 2π discontinuity errors in the unwrapped phase.

Several methods have been developed in the attempt to identify the corresponding dipoles and the route the branch-cuts have to go. The early algorithms used heuristic

arguments and non-optimum search strategies. In Buckland *et al* (1995) and Quiroga *et al* (1995) several techniques (simulated annealing, minimum-cost-matching, stable-marriages) are proposed for finding the corresponding dipoles with minimum total connection length, where the branch-cuts are assumed to be straight lines. The latter assumption leads to unrealistic discontinuities (cf figure 11).

These methods can be readily modified to accept cost functions associated with every segment of a branch-cut: Costantini (1996, 1998) and Flynn (1997) use techniques from graph theory and network programming to solve the following global minimization problem:

$$\min_{d_i, d_k} \left\{ \sum_i \sum_k c_i(i, k) |d_i(i, k)| + \sum_i \sum_k c_k(i, k) |d_k(i, k)| \right\} \quad (81)$$

subject to

$$2\pi \nabla \times \mathbf{d}(i, k) = -\nabla \times \hat{\nabla} \psi(i, k) \quad (82)$$

where

$$\begin{pmatrix} d_i(i, k) \\ d_k(i, k) \end{pmatrix} = \mathbf{d}(i, k) = \frac{1}{2\pi} (\nabla \hat{\phi}(i, k) - \hat{\nabla} \psi(i, k)) \quad (83)$$

as a (normalized) estimate of the phase gradient error $\mathbf{n}_\nabla(i, k)$ from equation (71). Its components are integers. It can be interpreted as an additive correction to $\hat{\nabla} \psi(i, k)$ applied before integration. Since, according to equation (82) the residue field of $\mathbf{d}(i, k)$ compensates the original residue field of the interferogram, the corrected gradient estimate is conservative and can be unambiguously integrated.

$c_i(i, k)$ and $c_k(i, k)$ are weighting (or cost) functions. They allow us to specify areas where the location of branch-cuts is likely (low cost) or unlikely (high cost). If the costs are chosen to be constant for all interferogram samples, equation (81) effectively minimizes the total cut-line length. More reasonable cost functions are based on estimates of local interferogram quality (e.g. coherence, phase gradient variance, residue density, etc). Figure 11 illustrates the influence of the cost function on the solution.

The solution that minimizes equation (81) is referred to as the minimum weighted discontinuity solution (Flynn 1997) or the minimum cost flow solution (Costantini 1996, 1998, Wu *et al* 1998). It gives an unwrapped phase whose gradient differs least from the original gradient estimate (in a weighted L^1 -norm sense).

4.5. Least squares estimation techniques

Weighted least squares estimation (LSE) algorithms (Ghiglia and Romero 1994, Herrmann 1980, Hunt 1979, Pritt and Shipman 1994, Song *et al* 1995, Spagnolini 1993, Takajo and Takahashi 1988) perform the following minimization:

$$\min_{\hat{\phi}} \left\{ \sum_i \sum_k |c(i, k) \cdot (\nabla \hat{\phi}(i, k) - \hat{\nabla} \psi(i, k))|^2 \right\} \quad (84)$$

where $c(i, k)$ is a weighting vector similar to the one in equation (81). In general, the solution is no longer congruent with the interferometric phase, i.e. $W\{\hat{\phi}(i, k)\} \neq \psi(i, k)$. Equation (84) is a variational problem whose Euler equation is—in the unweighted case—the well known Poisson equation:

$$\nabla \cdot \nabla \hat{\phi}(i, k) = \nabla \cdot \hat{\nabla} \psi(i, k) \quad (85)$$

under the Neumann boundary condition. For rectangular supports it can be solved by fast and simple cosine or Fourier transform filtering (Ghiglia and Romero 1994, Pritt and Shipman 1994). Also for the weighted case fast solutions are available (Pritt 1996).

It can be shown, that LSE is prone to severe errors caused by residues (Bamler *et al* 1998, Loffeld *et al* 1996). These errors propagate over the entire interferogram and distort the reconstructed phase globally. Also, due to the unconventional properties of phase gradient estimation noise mentioned in the slope bias section above, LSE tends to underestimate terrain slopes. Proper weighting can to some degree relieve these problems, but for correct phase reconstruction the weights must be chosen such that they are zero along the branch-cuts connecting the residues. Hence, also LSE techniques require knowledge about the branch-cut location. From that the usefulness of LSE phase unwrapping seems at least questionable.

An interesting relationship between unweighted LSE and 1D integration has been shown by Fornaro *et al* (1997). The unwrapped phase obtained by LSE is the average of the integration results of all possible integration paths disregarding residues and branch-cuts.

4.6. Other methods

A recently proposed Green's functions approach to phase unwrapping (Fornaro *et al* 1996) can be shown to be more or less equivalent to the LSE methods.

Especially for high coherence interferograms *region growing* phase unwrapping techniques have proven to give very good results (Reigber and Moreira 1997, Xu and Cumming 1996). They attempt to identify regions of high quality and unwrap them individually. In a second step these reliably unwrapped isolated areas are stitched together.

Kalman filters have been used for phase unwrapping (Krämer and Loffeld 1996, Loffeld *et al* 1996). They allow us to combine prefiltering for noise reduction, local frequency estimation and integration in an elegant fashion.

Multiresolution frequency estimators combined with LSE achieve asymptotically unbiased slope reconstruction (Davidson and Bamler 1996, 1998, Davidson *et al* 1993). They can locally adapt to interferogram quality and can adjust their horizontal resolution accordingly.

A more rigorous approach to phase unwrapping is obtained by considering the entire interferometric imaging mechanism and formulating the *Bayesian inference* problem of terrain reconstruction (Datcu 1996, Marroquin and Rivera 1995, Wilkinson and Datcu 1997). The instrument impulse response function, coherence properties, and phase and amplitude statistics can be used in a statistically optimum way in the likelihood term. Prior information about terrain properties (e.g. roughness or fractal dimension) constrains the solution.

Explicit phase unwrapping can sometimes be avoided, if several interferograms of the same area but acquired at different baselines are available (*multibaseline* approach) (Ferretti *et al* 1997). Then a MLE for the terrain height can be formulated as follows. Using ψ and a local estimate of coherence, the periodic phase likelihood function is known according to equation (59). It can be transformed into a likelihood for terrain height via the baseline-dependent factor of equation (28). Its period depends on the baseline which is in general different for the different interferograms. The product of these functions is the total likelihood function for terrain height. The location of its peak defines the MLE. Again, additional prior information about terrain may be used to improve the solution.

5. Interferometric configurations and examples

We have mentioned that the two SAR images forming an interferogram must differ in at least one imaging parameter; in the case of across-track interferometry the two images have been acquired from different orbit positions leading to different look angles θ_1 and

θ_2 . As a measure of the angular separation of the antennas we have used the term *baseline* $B_{\perp} \cong R\Delta\theta$.

Generalizing this concept we can also characterize other interferometric configurations by the type of ‘baseline’ they employ. If the two images have been acquired from the same flight path but at different times we may call the time lag a *temporal baseline* Δt . Likewise, a different radar frequency used for taking the two images can be denoted as *spectral baseline* Δk . We will discuss these three types of SAR interferometers separately, although in practice we often find mixed configurations, for example repeat-pass interferometers have both a spatial and a temporal baseline component. Table 1 summarizes the interferometric configurations.

Table 1. Possible InSAR configurations.

Baseline type	Interferometric configuration	Applications, measurement of . . .
$\Delta\theta$	across-track	topography
$\Delta t = \text{ms to s}$	along-track	ocean currents moving object detection
$\Delta t = \text{days}$ $\Delta t = \text{days to years}$	differential differential	glacier/ice field/lava flows subsidence seismic events volcanic activities crustal displacements
$\Delta t = \text{ms to years}$	coherence estimator	sea surface decorrelation time scene classification
Δk	Δk -radar	exact ranging of targets elimination of propagation medium effects

5.1. Across-track interferometry

In the preceding sections we have used across-track InSAR as the standard interferometric configuration (cf figure 6). In its pure form it requires a *single-pass/dual-antenna* arrangement where one antenna (the *master*) operates in receive/transmit mode while the *slave* antenna is in receive mode only. In this case the slave system is a bistatic SAR with its phase centre half-way between the two antennas; the effective baseline is only half the geometric distance of the antennas. Some single-pass interferometers operate in a ping-pong fashion where the role of master and slave antennas is exchanged at every pulse, thus avoiding the halving of the effective baseline.

The application of across-track interferometry is topographic mapping (figure 12). The height-to-phase sensitivity is given by equation (28).

The spatial separation of the antennas must be smaller than the critical baseline from equation (54) and, hence, is very small compared to the range. Therefore, the two wave propagation paths are almost identical and inhomogeneities of the propagation medium (ionosphere and atmosphere) cancel out in the interferometric phase. Since the two images are taken at the same time, temporal changes of scattering mechanisms do not enter the interferogram either. The only sources of decorrelation (i.e. of phase noise) are system noise, possible processing errors, and geometric decorrelation due to spectral shift and volume scattering (cf section 3). Spectral shift decorrelation and processing errors can be avoided

by careful processor design. Due to the lack of temporal scene decorrelation the coherence of single-pass interferograms is usually very high, e.g. $|\gamma| \geq 0.9$. If the system noise is known, the volumetric scattering contribution can be estimated from the interferogram coherence.

As will be seen in section 6 single-pass/dual-antenna systems are currently only found on aircrafts; comparable space-borne systems are not available. However, data from ERS-1/2 and other SAR satellites have been used extensively for DEM generation by means of repeat-pass interferometry (Hartl and Thiel 1993, Hartl *et al* 1994c). Due to the time delay between the two acquisitions the phase of such a *repeat-pass* interferogram contains the following (including unwanted) terms:

$$\phi = \phi_{\text{topo}} + \Delta\phi_{\text{prop}} + \Delta\phi_{\text{scat}} + \Delta\phi_{\delta R}. \quad (86)$$

Here, $\phi_{\text{topo}} \cong \frac{4\pi}{\lambda} \frac{B_{\perp}}{R \sin\theta} z$ is the wanted topography induced phase of equations (26) and (28).

$\Delta\phi_{\text{prop}}$ is a possible phase delay difference due to ionospheric and atmospheric propagation conditions (Goldstein 1995, Hanssen and Usai 1997, Massonnet *et al* 1995, Quegan and Lamont 1986, Tarayre and Massonnet 1994). Tropospheric water vapour and rain cells are dominant sources for this phase error. In ERS interferograms phase disturbances in the order of about half a fringe cycle (i.e. a quarter of a wavelength delay) are frequently encountered. Often the perturbations exhibit a turbulence-like structure; their power spectrum follows the well known $k^{-8/3}$ law (Ferretti *et al* 1997, Goldstein 1995).

$\Delta\phi_{\text{scat}}$ stands for the influence of any change in scattering behaviour. It may be a deterministic phase offset, e.g. due to a change in dielectric constant. It can also be a random phase as a consequence of temporal scene decorrelation.

$\Delta\phi_{\delta R} = \frac{4\pi}{\lambda} \delta R$ accounts for a possible displacement of the scatterer between observations, where δR is the projection of the displacement vector onto the line-of-sight (range) direction.

In the process of DEM generation from repeat-pass interferograms the mentioned disturbing terms are misinterpreted as terrain height z . Large baselines and/or averaging of several interferometric DEMs can combat this problem. An ERS interferogram taken, for example, at a baseline as large as 500 m (half the critical baseline) has a sensitivity of about one fringe cycle per 20 m terrain height reducing the influence of atmospheric disturbances to about 10 m. Optimum averaging of multiple interferograms exploits the special spectral nature of $\Delta\phi_{\text{scat}}$ (Ferretti *et al* 1997) and takes care of the local coherence. In practice, reliable DEM generation from repeat-pass interferometry requires several interferograms (typically 6–10) of the same area.

Temporal scene decorrelation finally governs the accuracy of repeat-pass InSAR. Depending on the type of terrain (dry solid rock versus forest) and the number of interferograms used height accuracies of 5–100 m at a spatial resolution of 25 m² are typical values for ERS-1/2 interferometry. Single-pass airborne systems can achieve accuracies and resolutions of less than a metre.

5.2. Along-track interferometry (ATI)

An along-track interferometer uses two antennas (transmit/receive and receive-only) separated by $2B_{\text{ATI}}$ arranged in flight direction (figure 31). Such a system takes two images of the same area at a time delay of $\Delta t = B_{\text{ATI}}/V$ where V is the sensor velocity. Typical values of Δt are 10–100 ms. If the scatterers were stationary between acquisitions the two data sets would be identical (save from noise) and the interferometric phase would be zero. Assume now that the scatterers in a resolution cell move at a velocity whose line-of-sight component is V_R . This leads to a relative range shift of the scatterers in the two images of

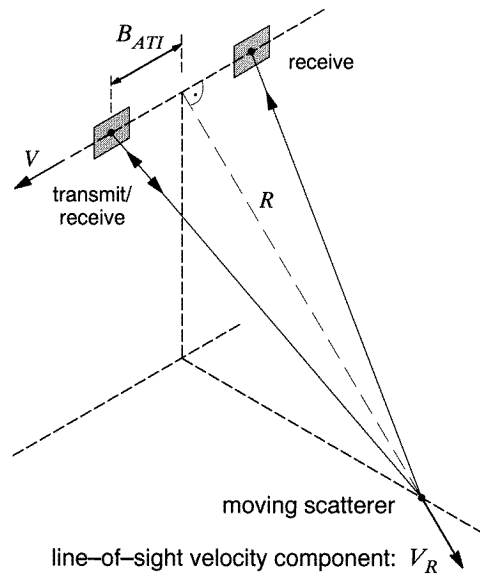


Figure 31. Along-track interferometer.

$\delta R = V_R \Delta t$ which transforms into an interferometric phase of

$$\phi_{ATI} = \frac{4\pi}{\lambda} \frac{B_{ATI} V_R}{V}. \quad (87)$$

Airborne ATI has been used for measurement of ocean currents (Bao *et al* 1997, Carande 1994, Goldstein *et al* 1989, Goldstein and Zebker 1987). Another possible application is traffic monitoring. ATI is closely related to moving target indication (MTI) for military use.

5.3. Differential interferometry (D-InSAR)

The temporal separation in repeat-pass interferometry of days, months, or even years can be used to advantage for long-term monitoring of geodynamic phenomena (Gabriel *et al* 1989, Thiel and Hartl 1993, Zebker and Rosen 1994). Any movement of a scatterer between the observations with a component of δR into the line-of-sight direction gives rise to an interferometric phase of

$$\Delta\phi_{\delta R} = \frac{4\pi}{\lambda} \delta R. \quad (88)$$

Since the wavelength is in the order of centimetres, D-InSAR can measure displacements down to millimetre accuracy—provided that coherence is high enough. Of course, all the phase terms of equation (86) contribute to D-InSAR measurements, but now $\Delta\phi_{\delta R}$ is the useful term and all the others should be eliminated.

Several methods have been developed to remove the topography induced phase. If an accurate DEM is available, ϕ_{topo} can be computed and subtracted from the interferometric phase. In place of a DEM a second interferometric data set can be employed if either a constant rate of displacement (e.g. glacier flow) or a singular motion event (e.g. earthquake) can be assumed. In either case the topographic phase can be separated from the motion contribution (Massonnet and Feigl 1995b, Massonnet *et al* 1996b).

Propagation medium effects $\Delta\phi_{prop}$ enter the D-InSAR measurement directly and can only be suppressed by averaging several observations.

A phase shift $\Delta\phi_{scat}$ due to changes in the scattering properties can be observed, for example, if soil moisture changed between observations. Often soil swells a few centimetres

when moistened and produces an additional phase shift $\Delta\phi_{\delta R}$. Depending on the soil material and the wavelength these effects may compensate each other or one of them dominates (Rudant *et al* 1996).

In the following application fields D-InSAR has been used successfully: measurement of glacier and ice sheet dynamics (Fahnestock *et al* 1993, Goldstein *et al* 1993, Hartl *et al* 1994a, Joughin *et al* 1995, Kwock and Fehnestock 1996, Thiel *et al* 1995, Thiel and Wu 1996, Wu *et al* 1997) (figures 13 and 14), seismic deformations (Feigl *et al* 1995, Massonnet and Feigl 1995a, Massonnet *et al* 1993, 1996a, Meyer *et al* 1996, Reigber *et al* 1997, Zebker and Rosen 1994) (figures 15 and 16), volcanic activities (Briole *et al* 1997, Massonnet *et al* 1995, Roth *et al* 1997, Thiel *et al* 1997), and land subsidence in mining areas (Massonnet *et al* 1997, Raymond and Rudant 1997). The advantage of D-InSAR compared to GPS networks is its dense sampling grid (every pixel is a measurement point) while GPS networks tend to undersample the displacement field. An overview of D-InSAR techniques is given in Klees and Massonnet (1997), Massonnet and Rabaute (1993).

5.4. Coherence evaluation

In this section we implicitly associated with the term *interferometric phase* its *mean* or expectation value. Coherence, or equivalently phase *variance*, is another valuable parameter that can be extracted from repeat-pass interferograms. As already mentioned, it provides information on the temporal stability of the subresolution scatterer structure and, hence, is an important feature for land cover classification (Askne and Smith 1996, Askne *et al* 1997, Borgeaud and Wegmüller 1996, Stebler *et al* 1996, Wegmüller and Werner 1997, Wegmüller *et al* 1995). Several reasons can lead to temporal decorrelation: changes in vegetation, freezing, thawing, movement of leaves due to wind, or human activities such as ploughing. Water surfaces decorrelate completely within tens of milliseconds, non-Gaussian discrete objects containing dominant scatterers tend to remain coherent over years (Usai 1997). Figures 17 and 18 illustrate how forest and different types of farmland can be separated by a local coherence estimate.

A simple model for decorrelation caused by random Gaussian displacement of subresolution scatterers is given in Zebker and Villasenor (1992):

$$\gamma_a = \exp \left\{ -\frac{1}{2} \left(\frac{4\pi}{\lambda} \right)^2 (\sigma_y^2 \sin^2 \theta + \sigma_z^2 \cos^2 \theta) \right\} \quad (89)$$

where σ_y^2 and σ_z^2 are the variances of the random motion components in ground range y and height z , respectively.

5.5. Δk -radar

SAR systems using different wavelengths from the same antenna position are usually referred to as Δk -radars rather than interferometers. They can be treated, however, by the methods presented in this paper. The interferometric phase of Δk -radar pixels can be thought as being generated by the beat frequency of the two microwaves; it is a highly accurate measure for range (in the subresolution regime). An interferometric equivalence of Δk -radars is given in Sarabandi (1997).

5.6. Important SAR system parameters

Besides the obvious interferometric configuration aspects such as baseline type and extent, several other SAR system parameters are important for SAR and InSAR applications and

require thorough consideration in the system design.

The radar frequency and, hence, the wavelength λ determines the antenna size, the technology for RF electronics and antennas and puts a limit to the available signal bandwidth. The sensitivity to unmodelled flight path perturbations increases with frequency. Longer wavelengths require larger baselines; note that the ratio B/λ is the deciding factor in the interferometric sensitivity constants of equations (28) and (87). The scattering mechanism depends on the wavelength in a complex way; even for mere surface scattering the backscattered power and, thus, the SNR in the image are strong functions of λ . A surface that is rough in X-band may be smooth and specular reflecting in P-band. When it comes to scatterer arrangements such as forests, the differences in radar signatures become even more pronounced: L-band penetrates canopy and is dominantly scattered from the soil with strong double-bouncing contributions from the trunks; C-band is mainly scattered by leaves and branches, while X-band almost does not penetrate the canopy and gets scattered at its outer boundary. P-band is the choice if substantial ground penetration is required. Temporal decorrelation increases rapidly with frequency according to equation (89). As a conclusion, for a (coherence-limited) repeat-pass InSAR system L-band ($\lambda \cong 24$ cm) is a preferred choice, while (baseline limited) single-pass/dual-antenna interferometers may use shorter wavelengths like X-band ($\lambda \cong 3$ cm).

The polarization of the transmitted and received wave is another parameter that has great influence on the radar signature of complex scatterers. The use of a fully polarimetric SAR allows for separation of different scattering mechanisms, e.g. surface, volume, and multiple scattering (Cloude and Pottier 1996). The combination of polarimetry and interferometry is a new field that promises a big step forward towards scene inversion (Cloude and Papathanassiou 1998, Hellman *et al* 1997, Papathanassiou and Cloude 1997).

Also the incidence angle θ determines the radar response of a scatterer. In most cases the backscattered power decreases with θ . Moreover, for a given altitude of the sensor the range increases with incidence angle and the SNR reduces. From the interferometric point of view θ should be chosen such as to balance the probability for lay-over and shadow and to move the 'blind angle' region towards less critical terrain slopes (cf figure 25). Hence, an incidence angle of about 45° is recommended.

The bandwidth of the transmitted pulse determines the range resolution of the system. Since excess resolution can be used to reduce phase noise by averaging, interferometric measurement accuracy benefits from high bandwidth as well. Bandwidth is limited by radar technology (price) and by CCIR regulations.

We have mentioned different imaging modes such as strip-map, ScanSAR, and spotlight as trade-offs between spatial resolution and coverage. Although high resolution is an obvious requirement, wide swath systems also have their advantages: given a satellite SAR that is required to image every point of the Earth, a wider swath width allows for a shorter revisit cycle. This in turn increases scene coherence and is favourable for repeat-pass InSAR.

6. Past, current and future InSAR systems

Interferometric SARs can be operated from aircraft or satellite. Airborne SARs with their single-pass capability are useful for regional high-accuracy topography mapping (down to the submetre range in all three dimensions) and (due to their comparably low flight velocity) for ocean current monitoring by ATI. Today, several such interferometric systems are operated by national organizations and private companies (Keydel 1996, Kramer 1996); TOPSAR (JPL, USA), IFSARE (ERIM/Intermap, USA), C/X-SAR (developed

Table 2. Spaceborne SAR systems suitable for interferometry. If not mentioned otherwise, spatial resolution is in the order of 5 m (azimuth) \times 25 m (ground range) and swath width 50–100 km.

Sensor	Mission period	Wavelength polarization	Mean incidence angle	Remarks
Repeat-pass systems				
SEASAT	1978	L HH	20°	first spaceborne SAR
SIR-C/X-SAR	1994 April and Oct.	L, C, X multipol	15–60°	first multifrequency, multipolarization SAR in space
ALMAZ-1	1991–1992	S	30–60°	
ALMAZ-1B	ca. 1998	P, S, X multipol	25–51°	
ERS-1	1991–today	C	23°	very accurate orbit
ERS-2	1995–today	VV		1 day revisit cycle during TANDEM missions
JERS	1992–today	L HH	35°	low S/N ratio due to hardware problems
Radarsat	1995–today	C HH	20–50°	multi-incidence angle multiresolution (10–1000 m) ScanSAR option
ENVISAT	ca. 1999	C HH, VV (VH) alternating	15–45°	multi-incidence angle very accurate orbit ScanSAR option
LightSAR	ca. 1999	L (C or X) HH, VH, VH HV	variable	short revisit cycles multi-incidence angle ScanSAR and spotlight options max. resolution: 1–3 m
Single-pass system				
SRTM	ca. 1999	C, X HH, VV	20–60°	dedicated InSAR mission single-pass system standard + ScanSAR modes

at CCRS, Canada), EMISAR (Technical University of Denmark), Ramses (ONERA, France), ESR (DERA, UK), DO-SAR (Dornier, Germany), E-SAR (DLR, Germany), AeS-1 (AeroSensing, Germany), AER-II (FGAN, Germany), a system by Sandia National Laboratories, Albuquerque, USA and one by CLR/NASDA, Japan.

In the remainder of this section we will concentrate on *spaceborne* SAR systems. They allow global mapping of topography and long-term monitoring of dynamic processes. Satellite data are at least one order of magnitude cheaper than airborne data. This is particularly true for inaccessible areas of the Earth.

Spaceborne remote sensing SAR sensors orbit the Earth at an altitude of typically 200 km (space shuttle) to 800 km (satellites) at inclinations ranging from 57° to 108°. Their spatial resolution is usually in the order of 5 m in azimuth and 25 m in ground range allowing for moderate averaging in azimuth for phase noise reduction to end up with square resolution elements of 25 m². The imaged swath is about 50–100 km wide in standard imaging mode and up to 500 km with ScanSAR systems. Table 2 summarizes some features of SAR satellites relevant for interferometry.

When judging the progress made so far in SAR interferometry it should be kept in mind

that neither of today's spaceborne SARs have been designed explicitly for interferometry. In particular, there will be no single-pass/dual-antenna system in space before the Shuttle Radar Topography Mission (SRTM) in 1999 (see below). Some of the current satellite SARs have a too steep look angle and/or provide inaccurate orbit data.

The first Earth observation satellite to provide SAR data suitable for interferometry was SEASAT. Launched in 1978, it was operated for 100 days where SAR data collection was limited to a period of 70 days. The interferometric usefulness of the SEASAT SAR data for topographic mapping was demonstrated 8 years later by Zebker and Goldstein (1986), and for detection and mapping of small elevation changes by Gabriel *et al* (1989). Those interferometric products were gained by repeat-pass interferometry from some specific segments of the SEASAT orbits, where the proper baseline conditions were met and in regions where the Earth's surface backscatter conditions were stable enough for acquisition of coherent SAR image pairs. Until 1992 only a few more publications on SEASAT InSAR followed, because of various reasons: SAR interferometry was still in an early development stage and not very widely known. SAR data were only available to a limited group of scientists, the required data processing was still very expensive, and appropriate facilities existed only at a few research centres. The SEASAT SAR was an analogue system, thus of modest stability and accuracy, which made processing even more difficult. Optical image correlation was applied for the generation of the standard images. The orbit determination was not very precise, which made baseline determination a special issue.

The two space shuttle missions Shuttle Imaging Radar SIR-A (1981) and SIR-B (1984) were essentially copies of the SEASAT SAR. The contribution of these missions to SAR interferometry is not dramatic; only one publication is known to the authors on interferometry with SIR-B data (Gabriel and Goldstein 1988).

The Shuttle Imaging Radar SIR-C/X-SAR, however, was a big step forward: a multifrequency, multipolarization SAR with excellent performance. It was flown twice, in April and October 1994 for 10 days each. 50 hours of SIR-C data on each of four polarization channels and 50 hours of X-band data have been collected.

The last three days of the October mission were devoted to repeat-pass interferometry; the shuttle's orbit was trimmed such that: (1) a 1-day repeat cycle was obtained and (2) the new orbit partially matched the one in April. This procedure provided interferometric data with revisit cycles of 1, 2, 3 days and 6 months. The acquired data set was of unparalleled value for extensive investigations on multifrequency, multipolarization, and multitemporal interferometry; see e.g. Coltelli *et al* (1996) and Lanari *et al* (1996). For the first time numerous parametric studies become possible concerning the effects of wavelength, incidence angle, polarization and baseline. The results were used to study and promote the solution of inverse problems in radar remote sensing (see, e.g. the special SIR-C/X-SAR issue of *IEEE Transactions on Geoscience and Remote Sensing* **33** (4) (1995) and Schmillius and Evans (1997)). One of the most exciting results concerning InSAR was the establishing of a new discipline: polarimetric interferometry (Cloude and Papathanassiou 1997, 1998, Hellman *et al* 1997, Papathanassiou and Cloude 1997).

As a final high point of the Shuttle Imaging Radar line, the Shuttle Radar Topography Mission SRTM will be launched in 1999 (Jordan *et al* 1996). This first spaceborne single-pass/dual-antenna across-track interferometer will reuse the existing SIR-C/X-SAR hardware augmented by a second set of receive antennas for the C- and X-band SARs mounted at the tip of a 60 m boom, which extends from the cargo bay. Compared with the experimental nature of the first missions SRTM is driven by a tight operational requirement: topographic mapping of the entire land mass within $\pm 60^\circ$ latitudes during an 11 days flight. The C-band interferometer will operate in a 4-beam ScanSAR mode in order to achieve the required

swath width of 225 km. The data product will be a consistent global DEM meeting the military DTED-2 standard (1" posting, about 10 m height accuracy). Due to its shorter wavelength and the non-ScanSAR mode of operation, the X-band data will provide DEMs of about twice that accuracy (Bamler *et al* 1996b) but of narrower swath. The X-band instrument will image about 70% of the area covered by the C-band interferometer.

Recalling past experiences, it must be emphasized that the real breakthrough in SAR interferometry was achieved through the European ERS-1 satellite and its follow-on ERS-2.

ERS-1 was launched in 1991. Apart from the extraordinary technical performance with respect to stability, calibration, etc, the following reasons were essential for the excellent results that have been achieved with SAR in the area of repeat-pass interferometry.

The satellite orbit was determined with dm and cm accuracy; the baseline control was very good and many orbit pairs met the baseline conditions for repeat-pass interferometry.

The satellite was operated in different orbit phases. During the commissioning phase and the so-called ice phase a repeat period of 3 days was chosen. Most of the time it was operated with a repeat period of 35 days, and during one year with a 168 days repeat orbit. The 3 days phase was very attractive, as temporal coherence was reasonably high over such short time periods for large areas. However, short revisit times are always in conflict with coverage and data acquisition was restricted to limited strips of the globe. The 35 day period was interesting from the coverage point of view, because the whole globe (except the polar regions) was imaged. However, only areas of very stable backscatter characteristics gave sufficient interferometric quality: coherence was reduced during such a long time particularly in vegetated areas. The 168 day period was not destined for interferometry; neither the baseline conditions nor the temporal conditions were favourable.

The ERS-1 mission was officially terminated in 1996, at the end of the TANDEM-mission (see below). The satellite is in hibernation and will be reactivated, if tandem operation is required. This was the case, for example, in late 1996 during the eruption of a volcano underneath the Vatnajökull glacier in Iceland (Roth *et al* 1997, Thiel 1997) and in 1997 for mapping of boreal forest in Siberia.

The ERS-2 SAR is identical to the one of ERS-1. The satellite was launched in 1995 and has the same orbit parameters as ERS-1. It continues the ERS-program with the 35-days repeat period.

Most important from the SAR-interferometry point of view was the TANDEM-mission (Duchossois and Martin 1995) during which ERS-1 and ERS-2 were operated in parallel. ERS-2 followed ERS-1 on the same orbit at a 35 min delay. Together with the Earth's rotation this orbit scenario assured that ERS-1 and ERS-2 imaged the same areas at the same look angle at a 1 day time lag. The orbits were deliberately tuned slightly out of phase such that a baseline of some 100 m allows for cross-track interferometry. This virtual baseline between ERS-1 and ERS-2 could be kept very stable, because both satellites were affected by similar disturbing forces. The first of several TANDEM missions was executed in May 1996.

The tandem scenario combined the best of two worlds: due to the short time lag of 1 day, interferograms formed from ERS-1/2 tandem data showed considerably higher coherence than data from any other orbit phase (Stebler *et al* 1996). The 35 days repeat cycle allowed for global coverage within this time frame.

Despite all the excellent scientific results obtained with ERS data, it should be kept in mind that the instrument had been designed for oceanographic imaging and, hence, uses a very steep incidence angle of only 23°. According to figure 25 this means that terrain slopes of higher than about 20° cannot be mapped. This renders such a system unsuitable for operational mapping of rugged terrain.

The next European satellite-borne SAR will be the ASAR system (Karnevi *et al* 1994) on board ENVISAT expected to be launched in 1999. It is a C-band system with considerably higher flexibility compared with the ERS-SARs. It provides a choice of two polarizations out of HH, VV and VH. Its variety of imaging modes (different incidence angles, standard and ScanSAR wide swath modes) resembles the ones of Radarsat (see below). Orbit and orbit data accuracy will be similar to ERS.

The launch of the ESA satellite ERS-1 was followed by the Japanese JERS satellite. It is presently the only L-band system in space. Although it is still operating, hardware problems had called for a reduction of transmit power and the instrument now has a degraded performance.

The commercial Canadian satellite RADARSAT (Ahmed *et al* 1990) was launched in 1995. In comparison with the ERS-SAR it can be operated in various imaging modes with regard to incidence angle, resolution and swath width. It is the first operational spaceborne to feature the ScanSAR mode. Due to this system flexibility Radarsat is very interesting for interferometric applications (Geudtner *et al* 1997). Unfortunately, the orbit and its maintenance are only of modest accuracy.

Future SAR and InSAR systems aim at smaller (allowing for multisatellite launchers), lighter (reduction of launch costs), cheaper, and more flexible design as well as shorter revisit cycles. At least two frequencies should be employed, a preferred choice being L-band (fully polarimetric) together with C- or X-band (HH + VV). Spotlight mode is considered for resolution in the 1–3 m range.

Especially for tactical military applications revisit cycles in the order of 15 min are required, calling for a fleet of satellites (see e.g. the *Starlite* concept (Fulghum and Anselmo 1997)).

These ambiguous aims shall be reached by several measures: innovative lightweight antenna technology, heritage from modular communication satellite hardware, and assembly-line production. The first of these innovative SARs will be NASA's LightSAR (cf table 2). It will feature synchronization capabilities for future operation of two LightSARs for single-pass interferometry.

A different concept of low-cost SAR systems is based on the reuse of television of digital audio satellite signals. Only a quasigeostationary receive-and-downlink satellite is required to form a bistatic SAR configuration (Prati *et al* 1997). Although resolution and SNR of such a system are moderate it is an interesting alternative for long-term monitoring, for example by D-InSAR techniques.

Acknowledgments

The authors would like to thank several individuals for their valuable support to this paper: Marc Walessa has read and corrected the manuscript thoroughly and critically; Nico Adam, Michael Eineder, Stefanie Gebhardt, Xiaoqing Wu, and Ye Xia have provided us with SAR images and interferograms; Karl-Heinz Thiel, Didier Massonnet, and Lars Ulander have contributed to the compilation of references.

References

- Ahmed S, Warren H R, Symonds D and Cox R P 1990 The Radarsat system *IEEE Trans. Geosci. Remote Sens.* **28** 598–602
- Allan T D 1983 *Satellite Microwave Remote Sensing (Ellis Horwood Series in Marine Science)* ed T D Allen (Chichester: Ellis Horwood) p 526

- Alpers W, Ross D B and Rufenbach C L 1981 On the detectability of ocean surface waves by real and synthetic aperture radar *J. Geophys. Res.* **86** 6481–98
- Askne J and Smith G 1996 Forest INSAR decorrelation and classification properties *FRINGE 96 ESA Workshop on Applications of ERS SAR Interferometry (Zürich)* <http://www.geo.unizh.ch/rsl/fringe96/>
- Askne J I H, Dammert P B G, Ulander L M H and Smith G 1997 C-band repeat-pass interferometric SAR observations of the forest *IEEE Trans. Geosci. Remote Sens.* **35** 25–35
- Bamler R 1992 A comparison of range-Doppler and wavenumber domain SAR focusing algorithms *IEEE Trans. Geosci. Remote Sens.* **30** 706–13
- Bamler R, Adam N, Davidson G W and Just D 1998 Noise-induced slope distortion in 2-D phase unwrapping by linear estimators with application to SAR interferometry *IEEE Trans. Geosci. Remote Sens.* **36** in press
- Bamler R and Davidson G W 1997 Multiresolution signal representation for phase unwrapping and interferometric SAR processing *Int. Geoscience and Remote Sensing Symp. IGARSS'97 (Singapore)* pp 865–8
- Bamler R, Davidson G W and Adam N 1996a On the nature of noise in 2-D phase unwrapping *Microwave Sensing and Synthetic Aperture Radar (Proc. SPIE)* ed G Franceschetti, C J Oliver, F S Rubertone and S Tajbakhsh (Bellingham: SPIE) pp 216–25
- Bamler R and Eineder M 1996 ScanSAR processing using standard high precision SAR algorithms *IEEE Trans. Geosci. Remote Sens.* **34** 212–18
- Bamler R, Eineder M and Breit H 1996b The X-SAR single-pass interferometer on SRTM: Expected performance and processing concept *EUSAR'96 (Königswinter)* pp 181–4
- Bamler R and Schättler B 1993 SAR data acquisition and image formation *SAR Geocoding: Data and Systems* ed G Schreier (Karlsruhe: Wichmann) pp 53–102
- Bao M, Brüning C and Alpers W 1997 Simulation of ocean waves imaging by an along-track interferometric synthetic aperture radar *IEEE Trans. Geosci. Remote Sens.* **35** 618–31
- Barber B C 1985 Theory of digital imaging from orbital synthetic-aperture radar *Int. J. Remote Sens.* **6** 1009–57
- Blackledge J M 1987 Theory of imaging with airborne synthetic aperture radar *Optik* **78** 1–11
- Boone B G, Scott A G, Shukla O B and Terry D H 1989 Optical processing for radar signal analysis *Johns Hopkins APL Tech. Dig.* **10** 14–28
- Borgeaud M and Wegmüller U 1996 On the use of ERS SAR interferometry for the retrieval of geo- and bio-physical information *FRINGE 96 Workshop on Applications of ERS SAR Interferometry (Zürich)* <http://www.geo.unizh.ch/rsl/fringe96/>
- Briole P, Massonnet D and Delacourt C 1997 Post-eruptive deformation associated with the 1986–87 and 1989 lava flows of Etna, detected by radar interferometry *Geophys. Res. Lett.* **24** 37–40
- Brown W M 1967 Synthetic aperture radar *IEEE Trans. Aerosp. Electron. Syst.* **AES-3** (2) 217–29
- Brown W M and Porcello L J 1969 An introduction to synthetic aperture radar *IEEE Spectrum* **September** 52–62
- Buckland J R, Huntley J M and Turner S R E 1995 Unwrapping noisy phase maps by use of a minimum-cost-matching algorithm *Appl. Opt.* **34** 5100–8
- Cafforio C, Prati C and Rocca F 1991 Full resolution focusing of Seasat SAR images in the frequency-wavenumber domain *Int. J. Remote Sens.* **12** 491–510
- Carande R E 1994 Estimating ocean coherence time using dual-baseline interferometric synthetic aperture radar *IEEE Trans. Geosci. Remote Sens.* **32** 846–54
- Carrara W G, Goodman R S and Majewski R M 1995 *Spotlight Synthetic Aperture Radar: Signal Processing Algorithms* (Boston, MA: Artech House)
- Cloude S R and Papathanassiou K P 1997 Coherence optimisation in polarimetric SAR interferometry *Int. Geoscience and Remote Sensing Symp. IGARSS'97 (Singapore)* pp 1932–4
- 1998 Polarimetric SAR-interferometry *IEEE Trans. Geosci. Remote Sens.* **36** submitted
- Cloude S R and Pottier E 1996 A review of target decomposition theorems in radar polarimetry *IEEE Trans. Geosci. Remote Sens.* **34** 498–518
- Coltelli M, Fornaro G, Franceschetti G, Lanari R, Migliaccio M, Moreira J R, Papathanassiou K P, Puglisi G, Riccio D and Schwäbisch M 1996 SIR-C/X-SAR multifrequency multipass interferometry: A new tool for geological interpretation *J. Geophys. Res.* **101** 23.127–13.148
- Costantini M 1996 A phase unwrapping method based on network programming *FRINGE 96 ESA Workshop on Applications of ERS SAR Interferometry (Zürich)* <http://www.geo.unizh.ch/rsl/fringe96/>
- 1998 A novel phase unwrapping method based on network programming *IEEE Trans. Geosci. Remote Sens.* **36** submitted
- Cumming I G, Guo Y and Wong F 1997 A comparison of phase-preserving algorithms for burst-mode SAR data processing *Int. Geoscience and Remote Sensing Symp. IGARSS'97 (Singapore)* pp 731–3
- Curlander J 1982 Location of spaceborne SAR imagery *IEEE Trans. Geosci. Remote Sens.* **GE-20** 359–64
- Curlander J C and McDonough R N 1991 *Synthetic Aperture Radar: Systems and Signal Processing* (New York:

- Wiley)
- Dainty J C 1975 *Laser Speckle and Related Phenomena* (Berlin: Springer) p 286
- Datcu M 1996 Maximum entropy solution for InSAR phase unwrapping *Int. Geoscience and Remote Sensing Symp.* '96 (Lincoln, NE) pp 310–14
- Davenport W B 1958 *Random Signals and Noise* (New York: McGraw-Hill)
- Davidson G W and Bamler R 1996 Robust 2-D phase unwrapping based on multiresolution *Microwave Sensing and Synthetic Aperture Radar (Proc. SPIE)* ed G Franceschetti, C J Oliver, F S Rubertone and S Tajbakhsh (Bellingham: SPIE) pp 226–37
- 1998 Multiresolution phase unwrapping for SAR interferometry *IEEE Trans. Geosci. Remote Sens.* **36** in press
- Davidson G W and Cumming I G 1997 Signal properties of spaceborne squint-mode SAR *IEEE Trans. Geosci. Remote Sens.* **35** 611–17
- Davidson G W, Cumming I G and Ito M R 1993 An approach for improved processing in squint mode SAR *Int. Geoscience and Remote Sensing Symp. IGARSS'93 (Tokyo)* pp 1173–5
- 1996 A chirp scaling approach for processing squint mode SAR data *IEEE Trans. Geosci. Remote Sens.* **32** 121–33
- Di Cenco A 1988 Strip mode processing of spotlight synthetic aperture radar data *IEEE Trans. Aerosp. Electron. Syst.* **24** 225–30
- Duchossois G and Martin P 1995 ERS-1 and ERS-2 Tandem Operations *ESA Bull.* **83** 54–60
- Elachi C 1988 *Spaceborne Radar Remote Sensing: Applications and Techniques* (New York: IEEE)
- 1991 Spaceborne imaging radars *Int. J. Imaging Syst. Technol.* **3** 167–85
- Fahnestock M A, Bindschadler R, Kwok R and Jezek K 1993 Greenland ice sheet surface properties and ice dynamics from ERS-1 synthetic aperture radar imagery *Science* **262** 1530–4
- Feigl K, Sergaent A and Jacq D 1995 Estimation of an earthquake focal mechanism from a satellite radar interferogram: application to the December 4, 1992 Landers aftershock *Geophys. Res. Lett.* **22** 1037–48
- Ferretti A, Prati C, Rocca F and Monti Guarnieri A 1997 Multibaseline SAR interferometry for automatic DEM reconstruction *3rd ERS Workshop (Florence)* <http://florence97.ERS-symposium.org/>
- Floury N, Le Toan T and Bruniquel J 1997 A study of SAR interferometry over forests: Theory and experiments *Int. Geoscience and Remote Sensing Symp. IGARSS'97 (Singapore)* pp 1868–70
- Floury N, Le Toan T and Souyris J C 1996 Relating forest parameters to interferometric data *Int. Geoscience and Remote Sensing Symp. IGARSS'96 (Lincoln, NE)* pp 975–7
- Flynn T J 1997 Two-dimensional phase unwrapping with minimum weighted discontinuity *J. Opt. Soc. Am. A* **14** 2692–701
- Fornaro G, Franceschetti G and Lanari R 1996 Interferometric SAR phase unwrapping using Green's formulation *IEEE Trans. Geosci. Remote Sens.* **34** 720–7
- Fornaro G, Franceschetti G, Lanari R, Sansosti E and Tesauro M 1997 How global and local phase unwrapping techniques are connected *Int. Geoscience and Remote Sensing Symp. IGARSS'97 (Singapore)* pp 878–80
- Fortuny J, Ohlmer E, Sieber A J, Pasquali P, Prati C and Rocca F 1994 Validating SAR interferometry applications by using EMSL *Int. Geoscience and Remote Sensing Symp. IGARSS'94 (Pasadena, CA)* pp 736–8
- Franceschetti G and Schirizzi G 1990 A SAR processor based on two-dimensional FFT codes *IEEE Trans. Aerosp. Electron. Syst.* **AES-26** 356–66
- Fulghum D A and Anselmo J C 1997 DARPA pitches small sats for tactical reconnaissance *Aviat. Week Space Technol.* **9** 29
- Gabriel A K and Goldstein R M 1988 Crossed orbit interferometry: theory and experimental results from SIR-B *Int. J. Remote Sens.* **9** 857–72
- Gabriel A K, Goldstein R M and Zebker H A 1989 Mapping small elevation changes over large areas: differential radar interferometry *J. Geophys. Res.* **94** 9183–91
- Gatelli F, Monti Guarnieri A, Parizzi F, Pasquali P, Prati C and Rocca F 1994 The wavenumber shift in SAR interferometry *IEEE Trans. Geosci. Remote Sens.* **32** 855–65
- Geudtner D, Vachon P W, Mattar K E and Gray A L 1997 RADARSAT repeat-pass SAR interferometry: Results over an arctic test site *Geomatics in the Era of RADARSAT GER'97 (Ottawa)*
- Ghiglia D C and Pritt M D 1998 *Two-dimensional Phase Unwrapping: Theory, Algorithms, and Software* (New York: Wiley)
- Ghiglia D C and Romero L A 1994 Robust two-dimensional weighted and unweighted phase unwrapping that uses fast transforms and iterative methods *J. Opt. Soc. Am. A* **11** 107–17
- Goldstein R 1995 Atmospheric limitations to repeat-track radar interferometry *J. Geophys. Res.* **22** 2517–20
- Goldstein R, Engelhardt H, Kamb B and Frohlich R M 1993 Satellite radar interferometry for monitoring ice sheet motion: Application to an Antarctic ice stream *Science* **262** 1525–30
- Goldstein R M, Barnett T P and Zebker H A 1989 Remote sensing of ocean current *Science* **246** 1282–5

- Goldstein R M and Zebker H A 1987 Interferometric radar measurement of ocean surface current *Nature* **328** 707–9
- Goldstein R M, Zebker H A and Werner C L 1988 Satellite radar interferometry: two-dimensional phase unwrapping *Radio Sci.* **23** 713–20
- Goodman J W 1976 Some fundamental properties of speckle *J. Opt. Soc. Am.* **66** 1145–50
- 1995 Statistical properties of laser speckle *Laser Speckle and Related Phenomena* ed J C Dainty (Berlin: Springer) pp 9–77
- Gough P T and Hawkins D W 1997 Unified framework for modern synthetic aperture imaging algorithms *Int. J. Imaging Syst. Technol.* **8** 343–58
- Graham L C 1974 Synthetic interferometer radar for topographic mapping *Proc. IEEE* **62** 763–8
- Hanssen R and Usai S 1997 Interferometric phase analysis for monitoring slow deformation processes *3rd ERS Workshop (Florence)* <http://florence97.ERS-symposium.org/>
- Harger R O 1970 *Synthetic Aperture Radar Systems: Theory and Design* (New York: Academic)
- Hartl P and Thiel K-H 1993 Radar interferometry—Basic concepts and applications *ISPRS 29 (Hanover)* pp 207–33
- Hartl P, Thiel K-H and Wu X 1994a Information extraction from ERS-1 SAR data by means of InSAR and D-InSAR techniques in Antarctic research *2nd ERS-1 Symp. (Hamburg)* pp 697–701
- Hartl P, Thiel K-H, Wu X, Doake C and Sievers J 1994b Application of SAR interferometry with ERS-1 in the Antarctic *ESA Earth Observation Q.* **43**
- Hartl P, Thiel K-H, Wu X and Xia Y 1994c Practical applications of SAR interferometry: experiences made by the institute of navigation *2nd ERS-1 Symp. (Hamburg)* pp 717–22
- Hasselmann K and Hasselmann S 1991 On the nonlinear mapping of an ocean wave spectrum into a synthetic aperture radar image spectrum and its inversion *J. Geophys. Res.* **96** 10,713–29
- Haykin S 1985 Radar signal processing *IEEE Acoust. Speech Sig. Process. Mag.* **April** 2–18
- Hellman M, Cloude S R and Papathanassiou K P 1997 Classification using polarimetric and interferometric SAR-data *Int. Geoscience and Remote Sensing Symp. IGARSS'97 (Singapore)* pp 1411–13
- Herrmann J 1980 Least-squares wave front errors of minimum norm *J. Opt. Soc. Am. A* **70** 28–35
- Hunt B R 1979 Matrix formulation of the reconstruction of phase values from phase differences *J. Opt. Soc. Am.* **69** 393–99
- Jin M Y and Wu C 1984 A SAR correlation algorithm which accommodates large-range migration *IEEE Trans. Geosci. Remote Sens.* **GE-22** 592–7
- Jordan R L, Caro E R, Kim Y, Kobrik M, Shen Y, Stuhr F V and Werner M U 1996 Shuttle radar topography mapper (SRTM) *Microwave Sensing and Synthetic Aperture Radar (Proc. SPIE)* ed G Franceschetti, C J Oliver, F S Rubertone and S Tajbakhsh (Bellingham: SPIE) pp 412–22
- Joughin I R, Winebrenner D P and Fahnestock M A 1995 Observation of complex ice-sheet motion in Greenland using satellite radar interferometry *Geophys. Res. Lett.* **22** 571–4
- Joughin I R, Winebrenner D P and Percival D B 1994 Probability density functions for multi-look polarimetric signatures *IEEE Trans. Geosci. Remote Sens.* **32** 562–74
- Just D and Bamler R 1994 Phase statistics of interferograms with applications to synthetic aperture radar *Appl. Opt.* **33** 4361–8
- Karnevi S, Dean E, Carter D J Q and Hartley S S 1994 Envisat's advanced synthetic aperture radar: ASAR *ESA Bull.* **76** 30–5
- Keydel W 1996 SAR technique and technology, its present state of the art with respect to user requirements *EUSAR'96 (Königswinter)* pp 19–24
- Klees R and Massonnet D 1997 Deformation measurements using SAR interferometry: Potential and limitations *Geologie en Mijnbouw* submitted
- Kramer H J 1996 *Observation of the Earth and its Environment* (Berlin: Springer)
- Krämer R and Löffeld O 1996 Presentation of an improved phase unwrapping algorithm based on Kalman filters combined with local slope estimation *FRINGE 96: ESA Workshop on Application of ERS SAR Interferometry (Zürich)* <http://www.geo.unizh.ch/rsl/fringe96/>
- Krogstad H 1992 A simple derivation of Hasselmann's nonlinear ocean-synthetic aperture radar transform *J. Geophys. Res.* **97** 2421–5
- Kwocik R and Fahnestock M A 1996 Ice sheet motion and topography from radar interferometry *IEEE Trans. Geosci. Remote Sens.* **34** 189–220
- Lanari R *et al* 1996 Generation of digital elevation models by using SIR-C/X-SAR multifrequency two-pass interferometry: The Etna case study *IEEE Trans. Geosci. Remote Sens.* **34** 1097–115
- Lee J-S, Hoppel K W, Mango S A and Miller A R 1994 Intensity and phase statistics of multilook polarimetric and interferometric SAR imagery *IEEE Trans. Geosci. Remote Sens.* **32** 1017–28
- Li F K and Johnson W T K 1983 Ambiguities in spaceborne synthetic aperture radar systems *IEEE Trans. Aerosp.*

- Electron. Syst.* **AES-19** 389–97
- Loffeld O, Arndt C and Hein A 1996 Estimating the derivative of modulo-mapped phases *FRINGE 96 ESA Workshop on Applications of ERS SAR Interferometry (Zürich)* <http://www.geo.unizh.ch/rsl/fringe96/>
- Lyzenga D R 1986 Numerical simulation of synthetic aperture radar image spectra for ocean waves *IEEE Trans. Geosci. Remote Sens.* **GE-24** 863–72
- Madsen S N 1986 Speckle theory: Modelling, analysis and applications related to synthetic aperture radar *PhD* Technical University of Denmark
- 1987 Spectral properties of homogeneous and nonhomogeneous radar images *IEEE Trans. Aerosp. Electron. Syst.* **AES-23** 583–8
- Marroquin J L and Rivera M 1995 Quadratic regularization functionals for phase unwrapping *J. Opt. Soc. Am. A* **12** 2393–400
- Massonnet D, Briole P and Arnaud A 1995 Deflation of Mount Etna monitored by spaceborne radar interferometry *Nature* **375** 567–70
- Massonnet D and Feigl K 1995a Satellite radar interferometric map of the coseismic deformation field of the $M = 6.1$ Eureka Valley California earthquake of May 17, 1993 *Geophys. Res. Lett.* **22** 1541–4
- 1995b Discrimination of geophysical phenomena in satellite radar interferograms *Geophys. Res. Lett.* **22** 1537–40
- Massonnet D, Holzer T and Vadon H 1997 Land subsidence caused by the East Mesa geothermal field, California, observed using SAR interferometry *Geophys. Res. Lett.* **24** 901–4
- Massonnet D and Rabaute T 1993 Radar interferometry: limits and potential *IEEE Trans. Geosci. Remote Sens.* **31** 455–64
- Massonnet D, Rossi M, Carmona C, Adragna F, Peltzer G, Feigl K and Rabaute T 1993 The displacement field of the Landers earthquake mapped by radar interferometry *Nature* **364** 138–42
- Massonnet D, Thatcher W and Vadon H 1996a Detection of postseismic fault zone collapse following the Landers earthquake *Nature* **382** 612–16
- Massonnet D, Vadon H and Rossi M 1996b Reduction of the need for phase unwrapping in radar interferometry *IEEE Trans. Geosci. Remote Sens.* **34** 489–97
- McDonough R N, Raff B E and Kerr J L 1985 Image formation from spaceborne synthetic aperture radar signals *Johns Hopkins APL Techn. Dig.* **6** 300–12
- Meyer B, Armijo R, Massonnet D, de Chabalière J B, Delacourt C, Ruegg C, Achache J, Briole P and Papanastassiou D 1996 The 1995 Grevena (Northern Greece) earthquake: Fault model constrained with tectonic observations and SAR interferometry *Geophys. Res. Lett.* **23** 2677–80
- Middleton D 1960 *Introduction to Statistical Communication Theory* (New York: McGraw-Hill)
- Milman A S, Scheffler A O and Bennett J R 1993 A theory of the synthetic aperture radar images of time-dependent scenes *J. Geophys. Res.* **98** 911–25
- Monti Guarnieri A and Prati C 1996 ScanSAR focusing and interferometry *IEEE Trans. Geosci. Remote Sens.* **34** 1029–38
- Monti Guarnieri A, Prati C and Rocca F 1994 Interferometry with ScanSAR *EARSel Newsletter* December 20
- Moore R K, Claassen J P and Lin Y H 1981 Scanning spaceborne synthetic aperture radar with integrated radiometer *IEEE Trans. Aerosp. Electron. Syst.* **17** 410–20
- Moreira A, Mittermayer J and Scheiber R 1996 Extended Chirp Scaling algorithm for air- and spaceborne SAR data processing in stripmap and ScanSAR image modes *IEEE Trans. Geosci. Remote Sens.* **34** 1123–36
- Munson D C, O'Brien J D and Jenkins W K 1983 A tomographic formulation of spotlight-mode synthetic aperture radar *Proc. IEEE* **71** 917–25
- Ouchi K and Burridge D A 1993 A unified theory on the focusing effect in SAR ocean wave imaging *Int. Geoscience and Remote Sensing Symp. IGARSS'93 (Tokyo)* pp 3–6
- Papathanassiou K P and Cloude S R 1997 Polarimetric effects in repeat-pass SAR interferometry *Int. Geoscience and Remote Sensing Symp. IGARSS'97 (Singapore)* pp 1926–8
- Plant W J 1992 Reconciliation of theories of synthetic aperture radar imagery of ocean waves *J. Geophys. Res.* **97** 7493–501
- Prati C and Rocca F 1993 Improving slant-range resolution with multiple SAR surveys *IEEE Trans. Aerosp. Electron. Syst.* **29** 135–44
- Prati C, Rocca F and Guarnieri A M 1989 Effects of speckle and additive noise on the altimetric resolution of interferometric SAR (ISAR) surveys *Int. Geoscience and Remote Sensing Symp. IGARSS'89 (Vancouver)* pp 2469–72
- Prati C, Rocca F and Monti-Guarnieri A 1997 Passive geosynchronous SAR system reusing backscattered digital audio broadcasting signals *IEEE Trans. Geosci. Remote Sens.* submitted
- Pritt M D 1996 Phase unwrapping by means of multigrad techniques for interferometric SAR *IEEE Trans. Geosci.*

- Remote Sens.* **34** 728–38
- 1997 Congruence in least-squares phase unwrapping *Int. Geoscience and Remote Sensing Symp. IGARSS'97 (Singapore)* pp 875–7
- Pritt M D and Shipman J S 1994 Least-squares two-dimensional phase unwrapping using FFT's *IEEE Trans. Geosci. Remote Sens.* **32** 706–8
- Quegan S and Lamont J 1986 Ionospheric and tropospheric effects on synthetic aperture radar performance *Int. J. Remote Sens.* **7** 525–39
- Quiroga J A, González-Cano A and Bernabeu E 1995 Stable-marriages algorithm for preprocessing phase maps with discontinuity sources *Appl. Opt.* **34** 5029–38
- Raney R K 1980 SAR processing of partially coherent phenomena *Int. J. Remote Sens.* **1** 29–51
- 1982a Processing synthetic aperture radar data *Int. J. Remote Sens.* **3** 243–57
- 1982b Review of spaceborne and airborne SAR systems *Agard Lecture Series* **182** 11.1–11.20
- Raney R K, Runge H, Bamler R, Cumming I G and Wong F H 1994 Precision SAR processing using chirp scaling *IEEE Trans. Geosci. Remote Sens.* **32** 786–99
- Raney R K and Vachon P W 1988 Synthetic aperture radar imaging of ocean waves from an airborne platform: focus and tracking issues *J. Geophys. Res.* **93** 475–86
- 1989 A phase preserving SAR processor *Int. Geoscience and Remote Sensing Symp. IGARSS'89 (Vancouver)* pp 2588–91
- Raymond D and Rudant J-P 1997 ERSI-SAR interferometry; potential and limits for mining subsidence detection *3rd ERS Workshop (Florence)* <http://florence97.ERS-symposium.org/>
- Reigber A and Moreira J 1997 Phase unwrapping by fusion of local and global methods *Int. Geoscience and Remote Sensing Symp. IGARSS'97 (Singapore)* pp 869–71
- Reigber C, Xia Y, Michel G W, Klotz J and Angermann D 1997 The Antofagasta 1995 earthquake: Crustal deformation patterns as observed by GPS and D-InSAR *3rd ERS Workshop (Florence)* <http://florence97.IERS-symposium.org/>
- Richman D 1971 *Three Dimensional Azimuth-correcting Mapping Radar* (USA: United Technologies Corporation)
- Rocca F, Prati C and Monti-Guarnieri A 1989 New algorithms for processing of SAR data 7998/88/F/FL(SC) ESA/ESRIN
- Rodriguez E and Martin J M 1992 Theory and design of interferometric synthetic aperture radars *IEE Proc.* **139** 147–59
- Roth A, Adam N, Schwäbisch M, Mischen B, Böhm C and Lang O 1997 Observation of the effects of the subglacial volcano eruption underneath the Vatnajökull glacier in Iceland with ERS-SAR data *3rd ERS Workshop (Florence)* <http://florence97.ERS-symposium.org/>
- Rudant J-P, Bedidi A, Calonne R, Massonnet D, Nesti G and Tarchi D 1996 Laboratory experiments for the interpretation of phase shift in SAR interferograms *FRINGE 96 ESA Workshop on Applications of ERS SAR Interferometry (Zürich)*
- Runge H and Bamler R 1992 A novel high precision SAR focusing algorithm based on chirp scaling *Int. Geoscience and Remote Sensing Symp. IGARSS'92 (Houston, TX)* pp 372–5
- Sarabandi K 1992 Derivation of phase statistics from the Mueller matrix *Radio Sci.* **27** 553–60
- 1997 Δk -radar equivalent of interferometric SARs: A theoretical study for determination of vegetation height *IEEE Trans. Geosci. Remote Sens.* **35** 1267–76
- Scheuer T E and Wong F H 1991 Comparison of SAR processors based on a wave equation formulation *Int. Geoscience and Remote Sensing Symp. IGARSS'91 (Espoo)* pp 635–9
- Schmullius C C and Evans D L 1997 Synthetic aperture radar (SAR) frequency and polarization requirements for applications in ecology, geology, hydrology and oceanography: a tabular status quo after SIR-C/X-SAR *Int. J. Remote Sens.* **18** 2713–22
- Song S M-H, Napel S, Pelc N J and Glover G H 1995 Phase unwrapping of MR phase images using Poisson equation *IEEE Trans. Image Process.* **4** 667–76
- Spagnolini U 1993 2-D phase unwrapping and phase aliasing *Geophys.* **58** 1324–34
- 1995 2-D phase unwrapping and instantaneous frequency estimation *IEEE Trans. Geosci. Remote Sens.* **33** 579–89
- Stebler O, Pasquali P, Small D, Holecz F and Nüesch D 1996 Analysis of ERS-SAR tandem time-series using coherence and backscattering coefficient *FRINGE 96 ESA Workshop on Applications of ERS SAR Interferometry (Zürich)*
- Takajo H and Takahashi T 1988 Least-squares phase estimation from the phase difference *J. Opt. Soc. Am. A* **5** 416–25
- Tarayre H and Massonnet D 1994 Effects of a refractive atmosphere on interferometric processing *Int. Geoscience and Remote Sensing Symp. IGARSS'94 (Pasadena, CA)* pp 717–19

- Thiel K-H and Hartl P 1993 Fields of experiments in ERS-1 SAR interferometry in Bonn and Naples *Int. Symp.—From Optics to Radar, SPOT and ERS-1 Applications (Paris)*
- Thiel K-H, Hartl P and Wu X 1995 Monitoring the ice movements with ERS SAR interferometry in the Antarctic region *2nd ERS Application Workshop (London)*
- Thiel K-H and Wu X 1996 Monitoring ice movement in Antarctica *Sixth Int. Offshore and Polar Engineering Conf. (Los Angeles, CA)* pp 401–5
- Thiel K-H, Wu X and Hartl P 1997 ERS-Tandem interferometric observation of volcano activities in Iceland *3rd ERS Workshop (Florence)* <http://florence97.ERS-symposium.org/>
- Tomiyasu K 1978 Tutorial review of synthetic-aperture radar (SAR) with applications to imaging of the ocean surface *Proc. IEEE* **66** 563–83
- 1981 Conceptual performance of a satellite borne, wide swath synthetic aperture radar *IEEE Trans. Geosci. Remote Sens.* **GE-19** 108–16
- Tough R J A 1991 Interferometric detection of sea ice surface features *Memorandum 4446* Royal Signals and Radar Establishment, UK
- Touzi R and Lopes A 1996 Statistics of the Stokes parameters and the complex coherence parameters in one-look and multilook speckle fields *IEEE Trans. Geosci. Remote Sens.* **34** 519–31
- Touzi R, Lopes A, Bruniquel J and Vachon P W 1997 Coherence estimation for SAR imagery *IEEE Trans. Geosci. Remote Sens.* submitted
- Ulander L M H and Hagberg J O 1995 Radiometric and interferometric calibration of ENVISAT-1 ASAR 172 Chalmers University of Technology, Göteborg, Sweden
- Usai S 1997 The use of man-made features for long time scale INSAR *Int. Geoscience and Remote Sensing Symp. IGARSS'97 (Singapore)* 1542–4
- Vachon P W, Krogstad H E and Paterson J S 1994 Airborne and spaceborne synthetic aperture radar observation of ocean waves
- Walker 1980 Range-Doppler imaging of rotating objects *IEEE Trans. Aerosp. Electron. Syst.* **16** 23–52
- Wegmüller U and Werner C L 1997 Retrieval of vegetation parameters with SAR interferometry *IEEE Trans. Geosci. Remote Sens.* **35** 18–24
- Wegmüller U, Werner C L, Nüesch D and Borgeaud M 1995 Forest mapping using ERS repeat-pass SAR interferometry *ESA Earth Obser. Q.* **49** 4–7
- Wilkinson A J and Datcu M 1997 Interferometric SAR topographic mapping, a Bayesian model-based approach *COMSIG 97*
- Wu C, Liu K Y and Jin M 1982 Modeling and a correlation algorithm for spaceborne SAR signals *IEEE Trans. Aerosp. Electron. Syst.* **AES-18** 563–74
- Wu X, Thiel K-H and Hartl P 1997 Estimating ice changes by SAR interferometry *3rd Int. Airborne Remote Sensing Conf. and Exhibition (Copenhagen)* pp 110–17
- Wu X, Thiel K-H, Hartl P and Kleusberg A 1998 Development in two dimensional phase unwrapping *IEEE Trans. Geosci. Remote Sens.* submitted
- Xu W and Cumming I 1996 A region growing algorithm for InSAR phase unwrapping *Int. Geoscience and Remote Sensing Symp. IGARSS'96 (Lincoln, NE)* pp 2044–6
- Zebker H A and Goldstein R M 1986 Topographic mapping from interferometric synthetic aperture radar observations *J. Geophys. Res.* **91** 4993–9
- Zebker H A and Rosen P 1994 On the derivation of coseismic displacement fields using differential radar interferometry: the Landers earthquake *Int. Geoscience and Remote Sensing Symp. IGARSS'94 (Pasadena, CA)* pp 286–8
- Zebker H A and Villasenor J 1992 Decorrelation in interferometric radar echoes *IEEE Trans. Geosci. Remote Sens.* **30** 950–9